Microstructure Observations of Turbulent Heat Fluxes in a Warm-Core Canada Basin Eddy

ELIZABETH C. FINE, JENNIFER A. MACKINNON, AND MATTHEW H. ALFORD

Scripps Institution of Oceanography, University of California, San Diego, La Jolla, California

JOHN B. MICKETT

Applied Physics Laboratory, University of Washington, Seattle, Washington

ABSTRACT

An intrahalocline eddy was observed on the Chukchi slope in September of 2015 using both towed CTD and microstructure temperature and shear sections. The core of the eddy was 6°C, significantly warmer than the surrounding −1°C water and far exceeding typical temperatures of warm-core Arctic eddies. Microstructure sections indicated that outside of the eddy the rate of dissipation of turbulent kinetic energy ε was quite low $\left[\mathscr{O}(10^{-10}–10^{-9})\,\mathrm{W\,kg^{-1}}\right]$. However, at the edges of the eddy core, ε was elevated to $\mathscr{O}(10^{-8})\,\mathrm{W\,kg^{-1}}$. Three different processes were associated with elevated ε. Double-diffusive steps were found at the eddy's top edge and were associated with an upward heat flux of $5\,\mathrm{W\,m^{-2}}$. At the bottom edge of the eddy, shear-driven mixing played a modest role, generating a heat flux of approximately $0.5\,\mathrm{W\,m^{-2}}$ downward. Along the sides of the eddy, density-compensated thermohaline intrusions transported heat laterally out of the eddy, with a horizontal heat flux of $2000\,\mathrm{W\,m^{-2}}$. Integrating these fluxes over an idealized approximation of the eddy's shape, we estimate that the net heat transport due to thermohaline intrusions along the eddy flanks was 2 GW, while the double-diffusive flux above the eddy was 0.4 GW. Shear-driven mixing at the bottom of the eddy accounted for only 0.04 GW. If these processes continued indefinitely at the same rate, the estimated life-span would be 1–2 years. Such eddies may be an important mechanism for the transport of Pacific-origin heat, freshwater, and nutrients into the Canada Basin.

1. Introduction

In the last decades Arctic sea ice has declined at an alarming rate, and this loss is expected to continue in the coming years (Carmack et al. 2015; Overland and Wang 2013). Ocean heat fluxes have been known to contribute to the growth–melt cycle of Arctic sea ice since the 1970s (Maykut and Untersteiner 1971); however, the pathways by which oceanic heat reaches Arctic sea ice are complex, and our knowledge is constrained by a lack of in situ observations (Carmack et al. 2015). Global climate model predictions have historically underestimated the rate of sea ice melt (Eisenman et al. 2011); better knowledge of the processes that bring oceanic heat into contact with sea ice is needed to improve both regional and global model predictions.

Heat can be stored in subsurface water masses in the Arctic Ocean because salinity is much more influential than heat in setting the density of water near the freezing temperature. In the western Arctic, the relatively warm Pacific Summer Water (PSW) and Atlantic Water (AW) masses are found at 40–100- and 200–400-m depth, respectively. PSW originates with flows through the Bering Strait, driven by the pressure gradient associated with the higher sea level in the Pacific than in the Arctic. In the summer, these flows are further modified in the Chukchi Sea, developing into two varieties of PSW (Rudels 2001). These are the relatively warm fresh Alaskan Coastal Water (ACW) and somewhat colder and saltier summer Bering Sea Water (sBSW) (Shimada et al. 2001; Pickart et al. 2005; Timmermans et al. 2014). ACW is modified by inflow from Alaskan rivers and is identified by a temperature maximum in a salinity range of 29–32.2, while sBSW is modified in the Bering Sea and identified by a temperature maximum in the salinity range of 32.2–33 (Timmermans et al. 2014). The lateral distribution of PSW is thought to play a role in regulating the extent of sea ice (Shimada et al. 2001, 2006;

Corresponding author: Effie Fine, ecfine@ucsd.edu

Steele et al. 2004; Pickart 2004; Woodgate et al. 2010; Watanabe 2011), although the mechanism for heat flux from PSW to the surface is unclear in the Canada Basin, where PSW is generally found more than 50 m from the surface and is usually separated from the mixed layer by strong haloclines (Toole et al. 2010). Prior studies suggest that while Atlantic-origin water contains more subsurface heat than PSW, stratification allows only very modest heat fluxes out of the Atlantic layer in the western Arctic (Padman and Dillon 1987; Timmermans et al. 2008a; Sirevaag and Fer 2012; Lincoln et al. 2016).

Eddies are ubiquitous in the Arctic and are frequently observed by both ships and drifting platforms (Hunkins 1974; Newton et al. 1974; Manley and Hunkins 1985; D'Asaro 1988b; Padman et al. 1990; Plueddemann et al. 1998; Münchow et al. 2000; Muench et al. 2000; Krishfield et al. 2002; Halle 2003; Pickart et al. 2005; Pickart and Stossmeister 2008; Timmermans et al. 2008b; Kadko et al. 2008; Kawaguchi et al. 2012; Zhao et al. 2014; Bebieva and Timmermans 2015; Pisareva et al. 2015; Kawaguchi et al. 2016). Intrahalocline eddies in the western Arctic are thought to form as a result of instabilities at the mouth of Barrow Canyon (D'Asaro 1988a; Shaw and Chao 2003; Watanabe 2011) and along the Beaufort and Chukchi Slope Currents (Hunkins 1974; Manley and Hunkins 1985; Muench et al. 2000; Chao and Shaw 2003; Pickart 2004; Pickart et al. 2005; Spall et al. 2008; Watanabe 2011). As they make their way into the Canada Basin, such eddies may play an important role in the transport and modification of Pacific-origin Arctic water masses (D'Asaro 1988a; Steele et al. 2004; Pickart 2004; Pickart et al. 2005; Pickart and Stossmeister 2008; Spall et al. 2008; Watanabe 2011).

In this paper, we describe an anomalously warm anticyclonic eddy observed on the Chukchi slope in September of 2015 (Figs. 1 and 2). The core of this eddy was quite warm (6°C) and close to the surface (40 m). This is significantly warmer than most previously described Arctic eddies (Manley and Hunkins 1985), although Kawaguchi et al. (2012) observed an eddy with similar properties in 2010. The core of the warm eddy had similar temperature–salinity properties to ACW (see section 3). Warm ACW enters the central Canada Basin via Barrow Canyon (D'Asaro 1988b; Münchow and Carmack 1997; Steele et al. 2004; Shroyer 2012), where it divides into the baroclinically unstable Beaufort shelfbreak jet (Rudels 2001; Steele et al. 2004; Pickart 2004; Nikolopoulos et al. 2009; von Appen and Pickart 2012) and Chukchi Slope Current (Corlett and Pickart 2017). Warm-core eddies likely form as a result of instabilities either at Barrow Canyon or along the topographically trapped currents. These warm and salty Chukchi slope

eddies are somewhat analogous to the small warm and salty Mediterranean eddies ("meddies"), which have been described since the 1980s (Armi and Zenk 1984; Armi et al. 1989; Ruddick 1992; Ruddick et al. 2010). Warm ACW eddies could play a significant role in the transport of Pacific-origin freshwater, nutrients, and heat into the Arctic basin, which could play a role in setting stratification, affect biological productivity, and impact the growth/melt of sea ice.

In the following analysis we focus primarily on the processes that remove heat from the eddy's core. Our goal is twofold: to identify the processes that cause heat flux out of the eddy observed in September 2015 and to quantify the net heat flux due to these processes. Our analysis indicates that the following three processes act to extract heat from the eddy (in order of increasing importance): 1) shear-driven mixing, 2) double-diffusive layering, and 3) net lateral heat fluxes along the flanks of eddies. Here we briefly introduce the candidate processes. In section 3b(1) we present the evidence that these processes are active in the eddy, and in section 3b(2) we consider their respective contributions to heat flux.

a. Shear-driven mixing

When the shear within a flow is high relative to local stratification, instabilities may occur, resulting in overturns and turbulent mixing. Shear is elevated above and below the core of an eddy owing to its rotation. Smaller-scale variation in shear may be due to the effects of internal waves, which are primarily driven by winds and tides. Mixing due to shear-driven turbulence has been observed to play an important role in setting heat fluxes in the Eurasian Arctic (Fer et al. 2010; Peterson et al. 2017; Meyer et al. 2017); however, shear is generally low in the western Arctic owing to weak tides and modest wind-forced near-inertial waves (D'Asaro and Morehead 1991; D'Asaro and Morison 1992; Pinkel 2005; Fer 2009).

b. Double-diffusive convection

Double-diffusive convection (DDC) is a common phenomenon in the Arctic Ocean (Neshyba et al. 1971; Melling et al. 1984; Padman and Dillon 1987, 1988, 1989, 1991; Kelley et al. 2003; Sundfjord et al. 2007; Lenn et al. 2009; Timmermans et al. 2008a; Polyakov et al. 2012; Sirevaag and Fer 2012; Kawaguchi et al. 2012, 2014; Bebieva and Timmermans 2015; Guthrie et al. 2015; Bebieva and Timmermans 2017) and has previously been observed above warm-core Arctic eddies (Padman and Dillon 1991; Padman 1994; Bebieva and Timmermans 2015; Kawaguchi et al. 2012) and PSW intrusions (Kawaguchi et al. 2014). DDC occurs when gravitationally
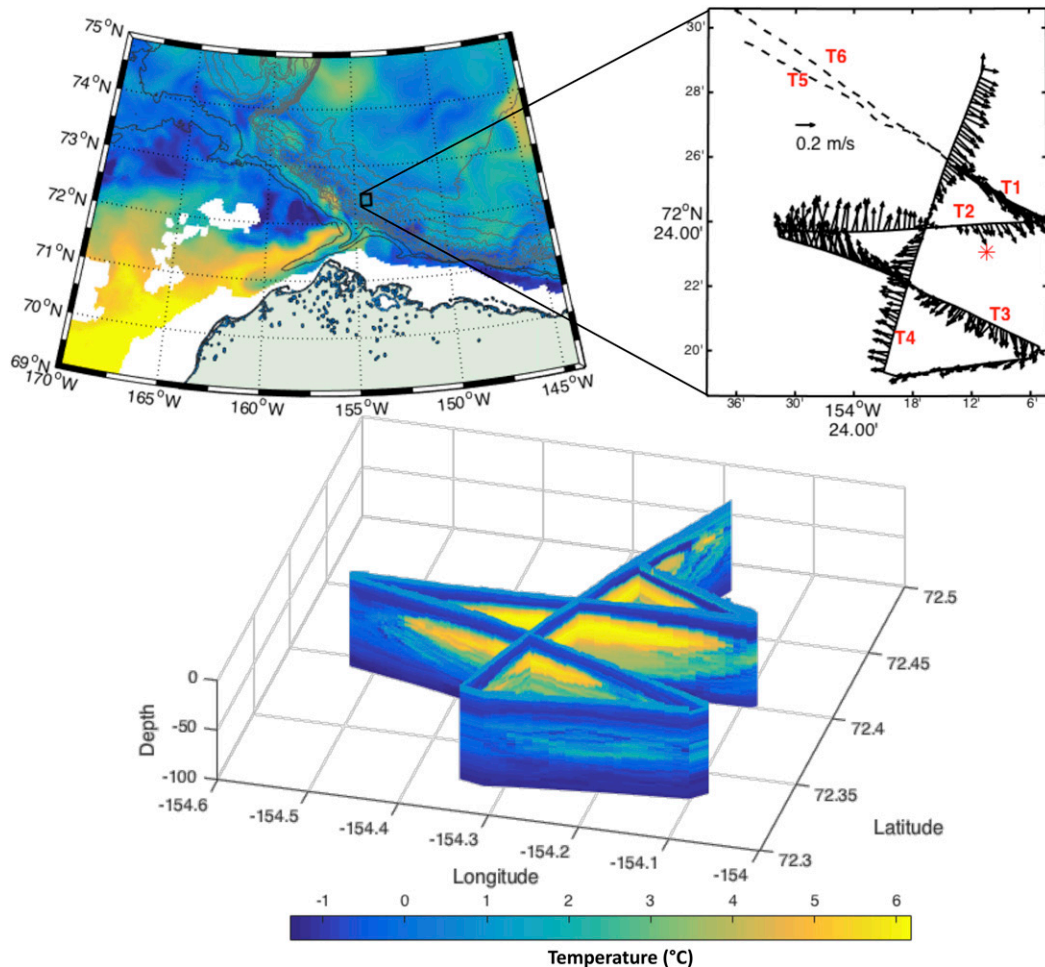
FIG. 1. Survey details. (left) Map of the Chukchi shelf slope. Color represents temperature at 50-m depth, as determined by a global HYCOM model (Metzger et al. 2014). Barrow Canyon is just to the northwest of Alaska. The eddy survey region is enclosed in a black box. (right) Eddy survey pattern. SWIMS sections are shown as solid lines, MMP as dashed. The average velocity relative to the eddy center in the 30–50-m depth range is shown for SWIMS sections. The red star indicates the inferred position of the eddy's center when the survey began. (bottom) Temperature measured in SWIMS survey along lines T1–T4.

stable cold and freshwater overlies a warm and salty layer. At a molecular level, heat diffuses upward faster than salt, leading to rising buoyant parcels. As a parcel rises, heat diffuses out of it faster than salt so that its buoyancy decreases. The parcel may initially overshoot its neutral density because of inertia, resulting in damped oscillatory behavior. Over time, this process results in well-defined convecting cells that are separated by thin interfaces where the cells meet. Fluxes of both heat and salt are generally continuous through layers and interfaces, but within the convecting layers both temperature and salinity are relatively uniform while across the interfaces there are sharp gradients in both temperature and salinity. This results in a characteristic staircase apparent in vertical profiles of

temperature, salinity, and density. DDC steps are ubiquitous in the Canada Basin above the Atlantic layer, but estimates of heat flux through them are fairly low, with an estimated range of 0.05–0.3 W m^{-2} (Timmermans et al. 2008a).

c. Lateral heat fluxes

Thermohaline intrusions occur where warm and salty water lies laterally next to cold and freshwater and are observed frequently throughout the world's oceans. These intrusions result in a net flux of heat and salt from the warm salty side of the front (Turner 1978; Ruddick and Richards 2003). Thermohaline intrusions have been observed at the edges of warm and salty Mediterranean eddies (meddies), where they dominate the decay of
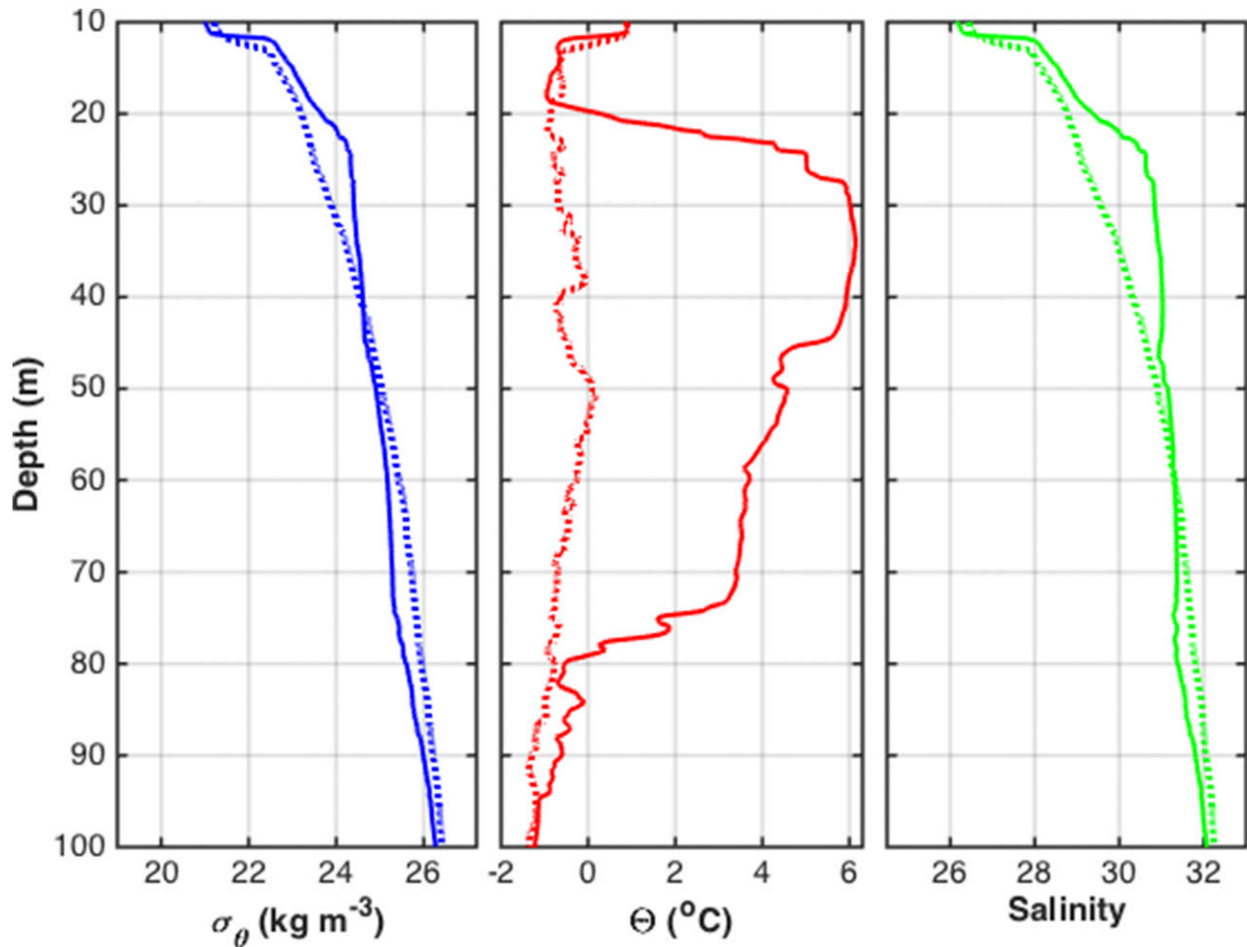
FIG. 2. (a) Potential density, (b) temperature, and (c) salinity within the eddy core (solid) and at a point outside of the eddy (dashed).

meddies' heat signature and density anomaly (Armi et al. 1989; Ruddick 1992; Ruddick et al. 2010). Similar intrusions have frequently been observed in the Arctic Ocean [see Ruddick and Richards (2003) for a review].

All three of these processes are known to occur in the Arctic, and the warm-core intrahalocline eddy described below contained regions in which each of them dominated local heat fluxes. However, the relative importance of these processes in the overall decay of warm intrahalocline eddies (or, more generally, subducted PSW) is not well understood, nor are the heat fluxes associated with each process. In the sections that follow, we describe the methods used to observe the eddy and outline the eddy's observed structure and properties. We describe the features that indicate the presence of different mixing processes and quantify the heat flux from the eddy's core due to each. Finally, we compare the relative importance of these processes and quantify the net heat transport out of the eddy's top, bottom, and sides.

2. Methods

The observations discussed in this paper were taken aboard the R/V *Sikuliaq* on the Chukchi slope in September of 2015. The survey was conducted just north of the mouth of Barrow Canyon at 72°23.17′N, 154°10.80′W. The first survey consisted of four Shallow Water Integrated Mapping System (SWIMS) transects, shown as solid lines in Fig. 1, and two Modular Microstructure Profiler (MMP) lines, shown as dashed lines in Fig. 1. Intermittent gaps in the MMP profiling occurred because of the MMP cable freezing to its reel. The number of profiles and speed during each transect are given in Table 1.

The observations discussed herein were obtained using two instruments both built by M. C. Gregg at the Applied Physics Laboratory of the University of Washington (APL/UW) and modernized and currently operated by our group at the Scripps Institution of Oceanography (SIO): SWIMS and MMP (Gregg and

TABLE 1. Description of each transect of the eddy survey undertaken using SWIMS and MMP. SWIMS is a towed profiler that carries both CTDs and ADCPs, while MMP has fast-response shear and temperature sensors to collect microstructure data. Transects are shown in Fig. 1.

Transect name	Instrument	Transect length (km)	No. of profiles	Ship speed (m s^{-1})
T1	SWIMS	7.2	34	2.1
T2	SWIMS	13.8	48	2.5
T3	SWIMS	16.3	97	1.7
T4	SWIMS	19.5	81	2.3
T5	MMP	15.1	40	0.5
T6	MMP	23.1	59	0.5

Pratt 2010; Wesson and Gregg 1994). SWIMS is a profiler that is towed behind a ship. It is rapidly winched up and down, making a tight sawtooth pattern. During the portions of this survey conducted using SWIMS, the ship maintained a speed of approximately 4 kt (2 m s^{-1}) over ground. Profiles (both up- and downcasts) were made to 150-m depth roughly every 100 s, corresponding to a horizontal resolution of ~200 m. SWIMS carries a Seabird 9plus CTD, upward- and downward-looking 300-kHz RDI workhorse ADCPs, an optical backscatter sensor, an oxygen sensor, a fluorometer, and an altimeter for work near the seafloor. Only CTD and ADCP data were used in the present study. Velocities were converted from relative to absolute values by vertically integrating shear and referencing the resulting velocities to a hull-mounted shipboard sonar. The CTD dataset used in this analysis was vertically gridded to 0.5-m bins, while the velocity dataset was gridded into 2-m bins. Velocities were determined to be unreliable within 20 m of the surface, owing to the ship wake and reflection from the surface; values in these depth bins are not reported.

MMP is a loosely tethered microstructure profiler. It falls at ~0.6 m s^{-1} and has two custom-built shear probes, an FP07 thermistor, CTD, and altimeter. The turbulent kinetic energy (TKE) dissipation rate ε was calculated from microscale shear measurements using an iterative process to fit a Panchev curve to the shear spectra, assuming isotropic turbulence (see Wesson and Gregg 1994). The dissipation rate of thermal variance χ was inferred from the FP07 assuming isotropic turbulence. Both ε and χ were windowed into 2.5-s segments (corresponding to 1–2 m in depth) prior to spectral analysis. Generally, $\chi = 6\kappa_T \langle \theta_z^2 \rangle$, in which κ_T is the molecular diffusivity of heat and $\langle \theta_z^2 \rangle$ is the variance of the thermal gradient. The fall rate of the MMP is too high to fully resolve the Batchelor spectra of the microstructure temperature gradients, so χ was inferred iteratively (Luketina and Imberger 2001). In each window, an initial estimate of χ was calculated by integrating the spectrum of θ_z. Maximum-likelihood estimation (MLE) was used with this χ estimate to determine the Batchelor wavenumber k_B (Ruddick et al. 2000). A revised estimate of χ was calculated from this k_B, and the process iterated until subsequent χ estimates were within 20% of the previous value. Because of the presence of submeter-scale structure in temperature, χ is very sensitive to the method of selection of spectral windows, with poorly selected windows introducing factor of 1000 errors into calculated χ. The procedure used to window χ is discussed in more detail in the appendix. The noise floors for ε and χ are 10^{-10} W kg^{-1} and 10^{-10}(°C)^2 s^{-1}, respectively. All MMP data were gridded to 0.25-m depth bins except where otherwise noted. For flux calculations, all quantities were smoothed in the vertical to 1 m. Bulk lateral thermal gradients were additionally smoothed laterally over 1 km.

Because of the lognormal distribution of ε and χ (e.g., Gregg et al. 1993), sampling errors in both directly measured quantities and calculated fluxes were determined using a bootstrapping procedure. The sampling errors in ε and χ were the largest source of quantifiable error in our calculated heat fluxes and were generally within 50% of the measured values. However, we cannot quantify errors due to instrument bias or violations of the assumptions inherent in the methods used to calculate heat flux, which likely have a bigger contribution to the uncertainties in mean quantities [e.g., Peters et al. (1988) report uncertainties of a factor of 2–3 in measured ε and χ]. All reported values are only accurate within a factor of 2–3, and for this reason, only one significant figure is reported for heat flux calculations.

3. Results

a. Eddy structure

CTD and ADCP data collected during the SWIMS transects indicate the eddy was an anticyclonic warm-core intrahalocline eddy, with core temperatures of 6°C (Figs. 1, 2, and 3). This is an exceptionally warm eddy for the Canada Basin, as most observed warm-core eddies
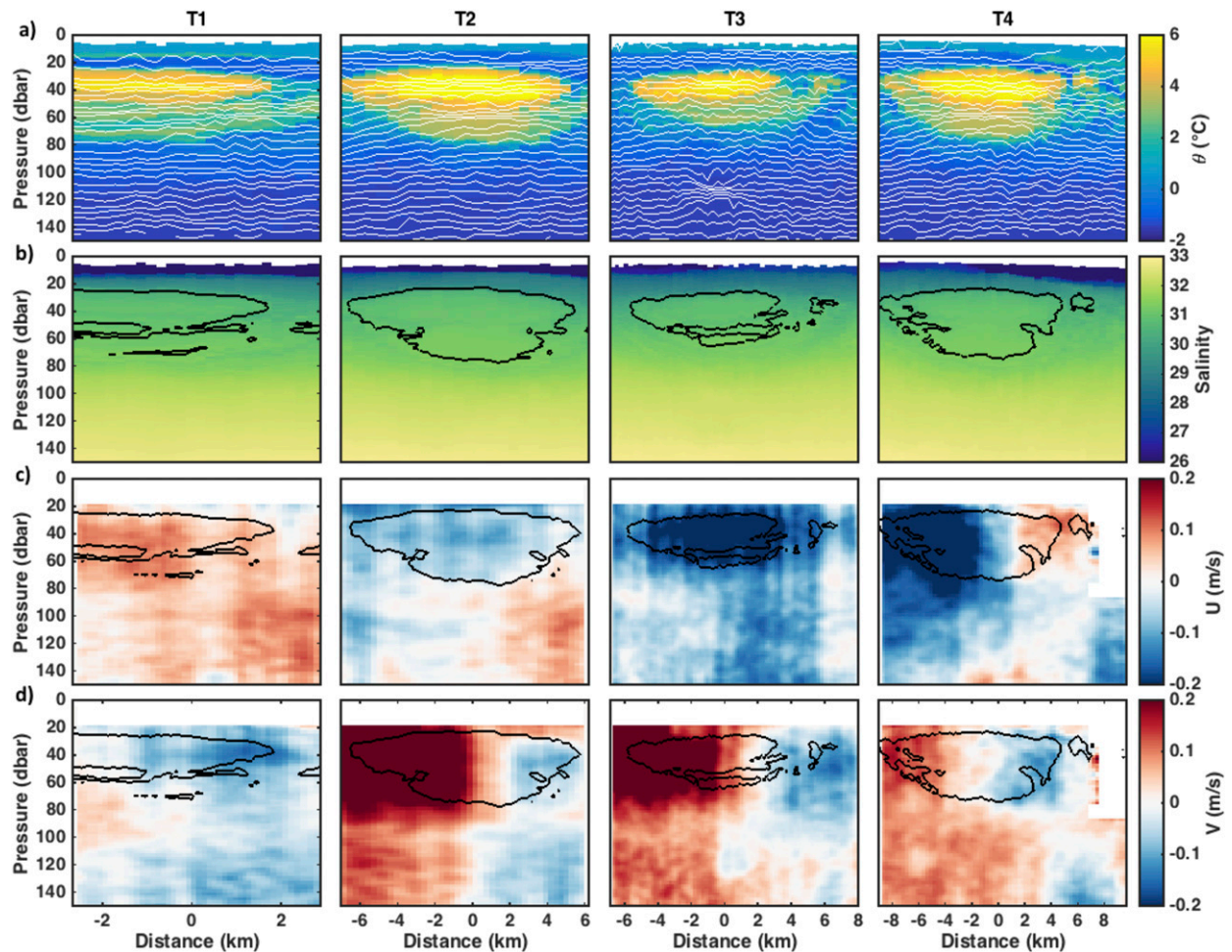
FIG. 3. SWIMS sections of (a) temperature, (b) salinity and (c) eastward and (d) northward velocity plotted against along-track distance. In (a), isopycnals are contoured in white. In (b), (c), and (d), the 3°C isotherm is contoured in black.

reach temperatures of 1°–2°C (Manley and Hunkins 1985; Pickart and Stossmeister 2008; Zhao et al. 2014). The eddy is warmest within 30–50-m depth, with a warm anomaly observed as deep as 95 m (Fig. 2).

Temperature and salinity measured in transects T1–T4 show a warm salty core (30–50 m) that was fairly homogeneous, although each transect captured different sections of this core (Fig. 3). Beneath this core, temperature decreased slowly, with the 3°C isotherm extending as deep as 75 m. In T3 and T4, a secondary warm anomaly appeared next to the eddy, likely part of an arm that extends off the eddy core. The salinity in the core of the eddy ranged from 31 to 31.5, which is within the salinity range for Alaskan Coastal Water (ACW) (Timmermans et al. 2014). The velocities measured are consistent with anticyclonic rotation (keeping in mind that most transects did not bisect the center of the eddy). The rotation of the eddy was apparent far beneath its warm core, with velocity signals extending as deep as

250 m, the deepest measurement (not shown). However, the warm core of the eddy from 30 to 50 m showed intensified velocities that were laterally offset from the rotation in the deeper portion of the water column.

Composite eddy features were determined by binning each measurement into overlapping 500-m bins based on radial distance from the eddy's center. To determine the eddy's center, all measurements were backtracked based on the average barotropic velocity during the survey of 4 cm s^{-1} north and 6 cm s^{-1} west. With the assumption that all points experienced this average velocity over the course of the survey, each point along the survey was backtracked to its position at the start of the survey. Using these new position coordinates for each measurement, the center was determined by least squares fitting to the location that minimized radial velocity (Fig. 1). The binned measurements were reflected about zero to create a composite transect through the eddy; Fig. 4 shows depth-averaged quantities for this composite transect.
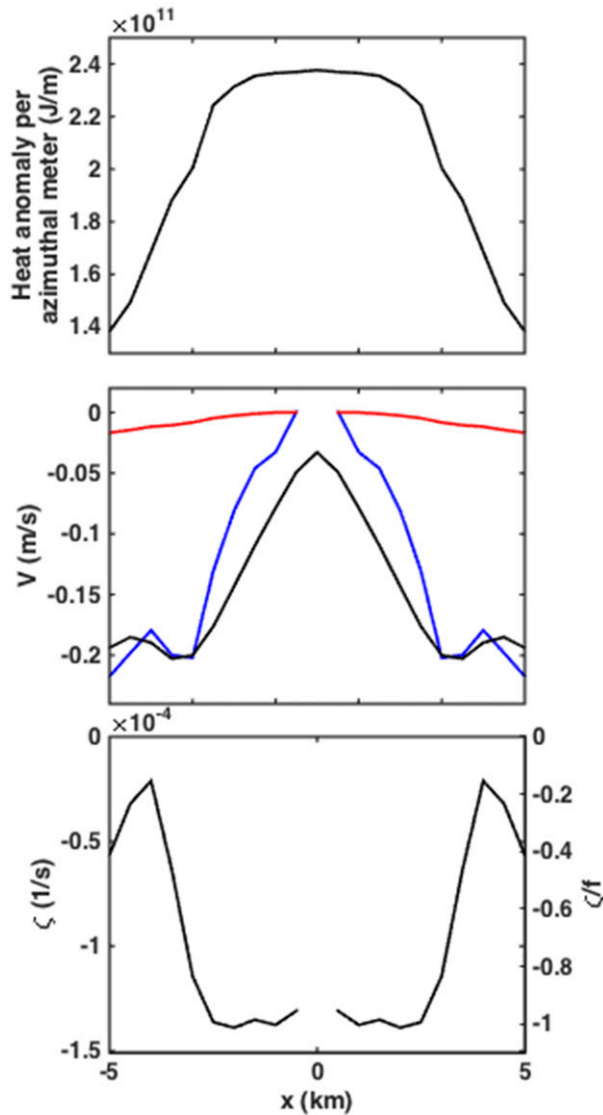
FIG. 4. Composite eddy (a) heat content anomaly relative to 0°C per azimuthal meter and (b) total (black), geostrophic (blue), and cyclostrophic (red) azimuthal velocity and (c) vorticity, averaged within the core of the eddy (30–50-m depth). Heat per meter in (a) is integrated vertically and radially, so that integrating azimuthally results in total eddy heat. All plots are symmetric about the center of the eddy.

Heat content anomaly per azimuthal meter relative to 0°C (Fig. 4a) was calculated in 500-m radial bins and was concentrated in the homogeneous warm core of the eddy. At the edges of the eddy, the heat anomaly tapered off. The total heat content anomaly of the eddy relative to 0°C of 7×10^{16} J was calculated by assuming azimuthal symmetry so that the heat calculated in each radial bin was integrated over a ring of equal distance from the eddy center.

Composite azimuthal velocity V_θ in each bin (Fig. 4b, black) was calculated by applying coordinate transforms

to each measured Cartesian velocity prior to binning these values. Geostrophic velocity $V_{\theta g}$ (Fig. 4b, blue) was determined by integrating the thermal wind equation,

$$\frac{\partial V_{\theta g}}{\partial z} = -\frac{g}{\rho_0 f} \frac{\partial \rho}{\partial r}, \tag{1}$$

in which g is acceleration due to gravity (9.8 m s^{-2}), r is the distance from a given bin to the eddy's center, f is 1.37×10^{-4} s^{-1}, and ρ is the binned potential density. We assumed completely geostrophic velocities at 140 m (the deepest we consistently sampled density). The $V_{\theta g}$ explained about 90% of the eddy's velocity, with cyclostrophic velocity ($V_{\theta c} = \sqrt{gr\rho_r/\rho}$; Fig. 4b, red) accounting for the remaining 10%.

The average relative vorticity $\zeta = r^{-1}\partial(rV_\theta)/\partial r$ across the full extent of the eddy (Fig. 4c) was -3×10^{-5} s^{-1}. Taking the eddy Rossby number to be Ro $= |\zeta|/f$ gives an eddy Rossby number of 0.2. Based on the Zhao et al. (2014) study of Arctic eddies identified from ice-tethered profiler (ITP) data, this is well within the range of eddies typically observed in the Arctic. Within the eddy's central core, the relative vorticity almost perfectly offsets planetary vorticity. This is similar to the eddy described by D'Asaro (1988b), in which the potential vorticity at the eddy core was nearly zero owing to the opposing influences of relative and planetary vorticity.

b. Turbulence and heat fluxes

Observations collected along transects T5 and T6 included microstructure shear and temperature measurements. All quantities were binned to 0.25-m bins with χ treated as discussed in the appendix. The lateral temperature gradient was smoothed over 1 km in the horizontal. The TKE dissipation rate (Fig. 5a) was high $[\mathcal{O}(10^{-6})\,\mathrm{W\,kg^{-1}}]$ near the surface (extending to 15–20-m depth) owing to ship wake and surface boundary layer processes (e.g., MacKinnon et al. 2016) and generally low beneath this layer. However, ε was elevated $[\mathcal{O}(10^{-8})\,\mathrm{W\,kg^{-1}}]$ compared to background noise $[\mathcal{O}(10^{-10})\,\mathrm{W\,kg^{-1}}]$ in a relatively thin layer surrounding the eddy's thermohaline core. Within the core, ε was generally not detectable above the instrument noise level. Similarly, χ (Fig. 5, top right) was high near the surface and elevated at the edges of the eddy.

Elevated ε and high temperature gradients surrounding the eddy core (Figs. 5 and 3) suggest that heat may have been mixing from the eddy's core into the surrounding water. In the following section, we describe the observations that indicate the presence of three distinct processes: shear-driven mixing, DDC, and lateral heat fluxes due to thermohaline intrusions.
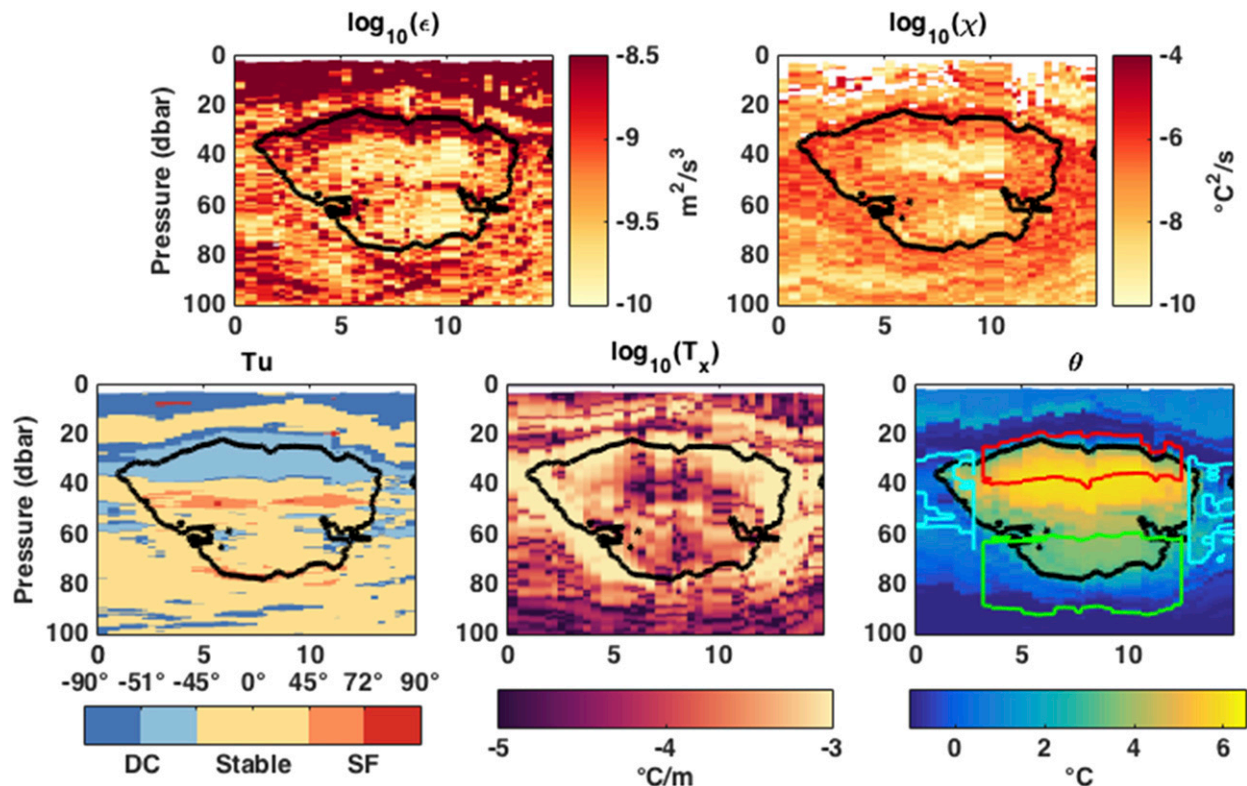
FIG. 5. The (a) ε, (b) χ, (c) vertical Turner angle, (d) horizontal temperature gradient, and (e) θ measured in T5. The x axis represents distance from the start of the transect (km). The 3°C isotherm is contoured in black; the zones referred to as the top, sides, and bottom of the eddy are contoured in red, cyan, and green, respectively, in (e).

This discussion is followed by a quantitative analysis of the heat fluxes and transport due to each process.

1) OBSERVATIONS INDICATING THE PRESENCE OF EACH PROCESS

(i) Shear-driven mixing

We calculated shear at a 4-m scale ($\mathbf{U}_{z_{4m}} = \sqrt{u_z + v_z}$) by interpolating velocity to a regularly spaced 0.2-km grid, smoothing to 4-m bins in the vertical and 1-km bins in the horizontal, and taking 4-m first differences. Above and below the eddy core, $\mathbf{U}_{z_{4m}}$ was elevated (Fig. 6a). The general pattern of $\mathbf{U}_{z_{4m}}$ was consistent with a core in solid-body rotation; however, there were smaller anomalies in shear that could be due to small-scale processes. Prior studies suggest that internal waves may interact with the potential vorticity of eddies, leading to effects that can induce refraction or wave breaking at the edge of eddies via various mechanisms (Kunze 1985, 1986), and such effects have been observed in previous studies of Arctic eddies (Halle 2003; Kawaguchi et al. 2016). The anomalies we observed in shear are suggestive of internal waves, although frequency information cannot be determined from this survey.

The buoyancy frequency squared N_{4m}^2 (Fig. 6b), similarly calculated by interpolating density to the same grid as velocity, smoothing, and taking first differences over 4 m, was also high above the eddy. The inverse Richardson number ($\mathrm{Ri}_{4m}^{-1} = \mathbf{U}_{z_{4m}}^2 / N_{4m}^2$) is used to characterize the propensity for shear instability, with growing instabilities expected for $\mathrm{Ri}^{-1} > 4$. In these measurements, Ri_{4m}^{-1} is generally low but is elevated below the eddy core, suggesting possible susceptibility to shear instabilities (Fig. 6c). Shear instabilities may also occur at vertical scales smaller than the 4-m smoothing used to calculate Ri_{4m}^{-1}. The rate of turbulent dissipation ε, measured on T5 using the MMP, was elevated above and beneath the eddy's core and on the flanks of the eddy (Fig. 6d). Beneath the eddy core, elevated ε may be explained by shear instabilities that occur as a result of geostrophic shear. However, the elevated ε above the eddy and on its flanks is primarily due to other smaller-scale processes.

(ii) DDC

The vertical temperature gradient just above the eddy's core was quite strong $\left[\mathcal{O}(1)°\mathrm{C}\,\mathrm{m}^{-1} \right]$ (Figs. 2a and 3).
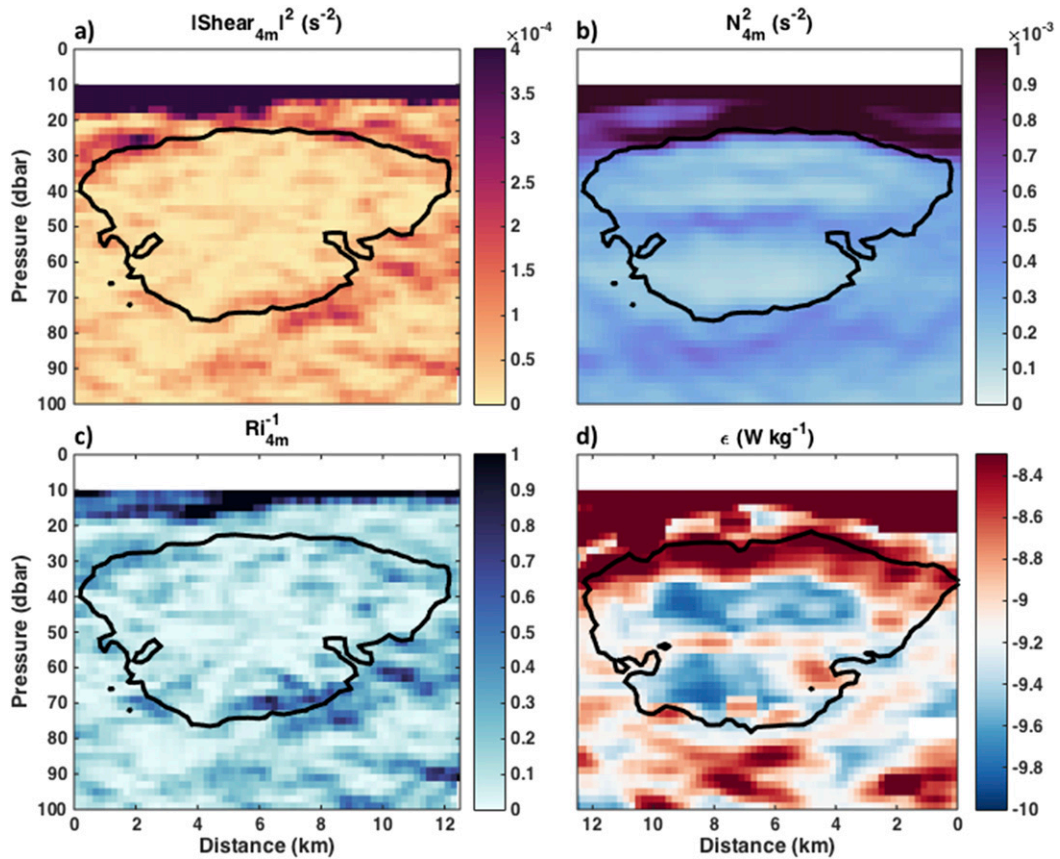
FIG. 6. (a) Magnitude-squared of shear$_{4m}$, (b) N^2_{4m}, and (c) inverse Ri$_{4m}$ from T2; (d) ε from T5. The 3°C isotherm is contoured in black in all panels. The x axis represents distance along each transect; in (d) the axis is flipped because T5 was undertaken in the opposite direction from T2. Although T2 and T5 do not spatially overlap (Fig. 1), the shape of the 3°C contour was similar in both transects owing in part to the eddy's translational motion during the survey.

Both temperature and salinity increased with depth above the eddy, creating favorable conditions for the formation of diffusive layers. These layers were apparent in individual profiles of both temperature and salinity (Figs. 7a,b) as well-mixed homogeneous layers separated by sharp interfaces with high gradients in both temperature and salinity.

The density ratio $R_\rho = (\beta \Delta S)/(\alpha \Delta T)$, in which α is the thermal expansion coefficient, β is the saline contraction coefficient, ΔT is the vertical difference in temperature over a given depth range, and ΔS is the vertical difference in salinity across the same range, indicates susceptibility to double diffusion (Turner 1974; Huppert and Turner 1981). The Turner angle (Fig. 5c) Tu $= \tan^{-1}[-(\alpha \Delta T)/(\beta \Delta S)] - 45°$ maps the density ratio onto the polar plane. In this formulation, $-90° <$ Tu $< -45°$ corresponds to DDC instabilities, $-45° <$ Tu $< 45°$ corresponds to stable stratification, $45° <$ Tu $< 90°$ indicates salt fingering instabilities, and Tu $> 90°$ and Tu $< -90°$ both correspond to gravitational instabilities. The Turner angle

indicates that the region above the eddy is subject to DDC, while the region within the eddy core is double-diffusively stable (Fig. 5c), consistent with the observed staircase structure at the top of the eddy (Fig. 7a). The average density ratio in this region is $R_\rho = 2.6 \pm 1.0$. Additional DDC characteristics are given in Table 2. Based on the presence of stair steps, shear that is weak relative to the local stratification, and the local Turner angle, we assume the elevated values of ε observed at the top of the eddy (Figs. 6 and 5) were associated primarily with DDC. There was a small region below the eddy's core that was weakly susceptible to salt fingering instabilities (75–80 m); however, since this region was quite small we conclude that shear-driven mixing was dominant beneath the eddy core. Salt fingering may have played a more significant role within the eddy core between 55- and 60-m depth; however, as this process moves heat within the eddy's core rather than removing it from the eddy we have not treated it in our analysis.
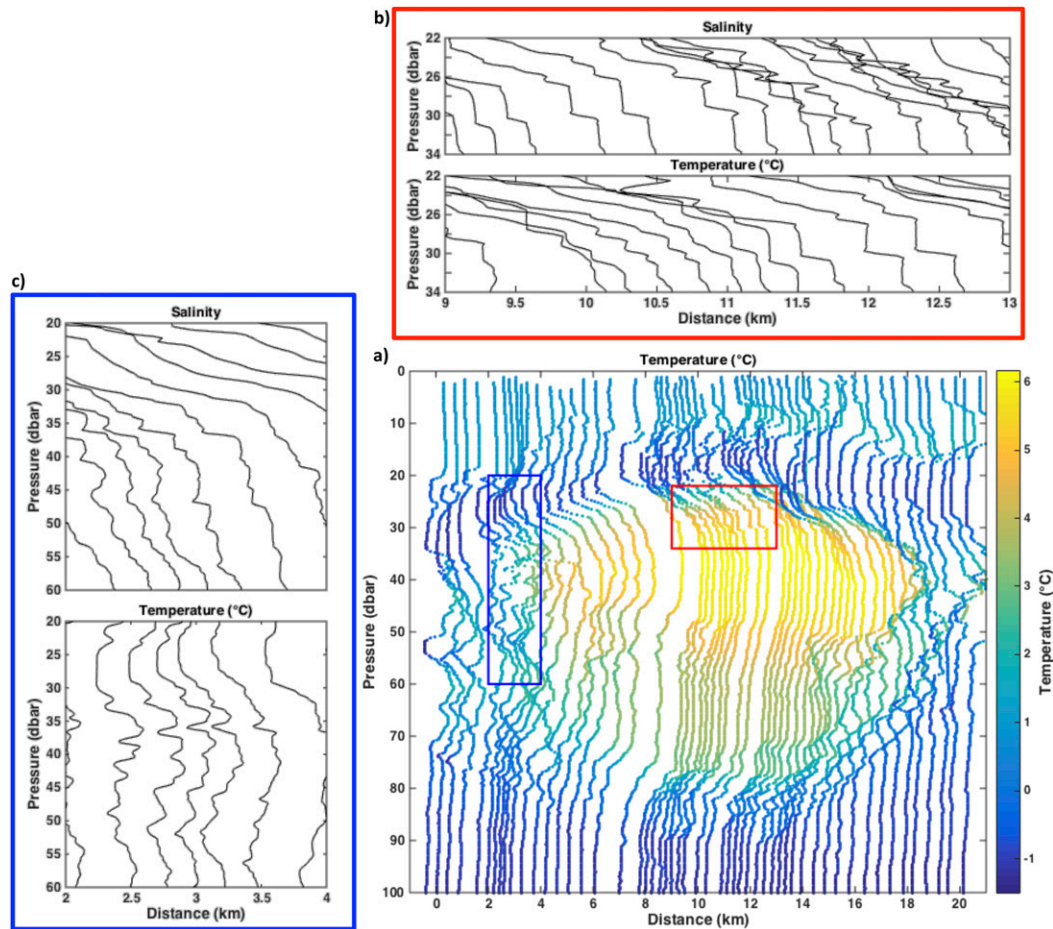
FIG. 7. Temperature and salinity profiles. (a) All temperature profiles taken on T5 of the eddy. The red box highlights a region with diffusive layers; the blue box highlights a region with thermohaline intrusions. (b) Salinity and temperature profiles at the top of the eddy. Distinctive steps are apparent, with well-mixed layers separated by sharp interfaces. The salinity profiles show some salinity spiking due to the abruptness of the interfaces. (c) Salinity and temperature profiles at the side of the eddy. Alternating layers of cold/fresh and warm/salty water indicate the presence of lateral intrusions.

(iii) Lateral intrusions

Lateral temperature gradients (Fig. 5d) and salinity gradients (not shown) were fairly strong along the sides of the eddy, with temperature gradients of $\mathcal{O}(10^{-3})°C\,m^{-1}$. This promotes another double-diffusive phenomenon: thermohaline intrusions. These intrusions appeared as alternating layers of cold–fresh and warm–salty water, which were coherent across multiple profiles at the sides of the eddy (Figs. 7a,c). Double-diffusive intrusions can occur because of the presence of warm salty water lying next to cold freshwater (Stern 1967; Ruddick and Turner 1979), and May and Kelley (1997) describe how a density-compensated thermohaline gradient, combined with lateral shear, can also trigger a baroclinic instability, leading to lateral mixing. The analysis that follows depends on the assumption that the intrusions were approximately in

steady state balance on time scales that are short relative to the eddy decay time, that is, that the time scale for the evolution of intrusions was significantly longer than the time scales associated with the observed turbulence (but short enough that the eddy did not decay substantially during this time scale). Intrusions generally evolve over

TABLE 2. Properties of DDC staircases. Means are taken over each step included in analysis. The 95% confidence intervals assuming statistically independent measurements are given in parentheses.

Property	Mean value (95% confidence interval)
R_ρ	2.6 (1.6, 3.6)
Layer height	0.96 m (0.88 m, 1.03 m)
Interface height	0.079 m (0.075 m, 0.083 m)
ΔT across interfaces	0.29°C (0.27°C, 0.31°C)

time scales of days to months (e.g., Gregg 1980; Armi et al. 1989), supporting this assumption.

A single vertical profile through the intrusive region shows the layered cold–fresh/warm–salty structure (Fig. 8a; this structure is more pronounced in temperature than salinity because of the higher resolution in temperature and its weaker influence on density). The Turner angle calculated along the profile shows both the top and bottom of warm–salty intrusions are susceptible to double diffusion, with DDC instability above intrusions and susceptibility to salt fingering beneath intrusions (Fig. 8b). We see evidence of DDC at the top of warm–salty regions, where small steps in both temperature and salinity indicate the presence of DDC (Fig. 8a). The rate of dissipation of both TKE and thermal variance was generally modest along intrusions, with intermittent spikes in both ε and χ apparent in diffusive convective regions (e.g., 60-m depth; Figs. 8c,d).

As intrusions develop along the flanks of an eddy, they act like the ribs on a radiator, increasing the surface area over which heat can exit the eddy. Along each warm–salty intrusion, strong thermal gradients above and below the intrusion drive double diffusion and allow heat to mix vertically out of the intrusion. If the intrusions remain in approximate steady state on time scales short compared to the eddy decay time, the total flux of heat out the top and bottom of each intrusion must be balanced by the lateral advective flux of heat along the warm–salty intrusion (just as the heat that radiates out of the ribs of a radiator must be balanced by heat that enters through the radiator's pipe if the radiator's temperature remains constant). This model has been used by Gregg (1980) and Ruddick et al. (2010) to infer the net lateral heat flux through intrusions by matching it to the small-scale turbulent heat fluxes through the edges of individual intrusions. This is the approach we take here as well.

2) HEAT FLUXES DUE TO EACH PROCESS

In the following analysis, each process is considered separately in the region of the eddy in which it dominates:

1) shear-driven turbulence beneath the eddy's core (horizontal coordinate $8 \, \text{km} < s < 16 \, \text{km}$ and $27 \, \text{km} < s < 35 \, \text{km}$, where s is kilometers along ship track from the start of the microstructure survey and within isopycnals $24.8 < \sigma_\theta < 25.5$; green contour in Fig. 5),

2) DDC ($8 \, \text{km} < s < 16 \, \text{km}$ and $27 \, \text{km} < s < 35 \, \text{km}$, where s is kilometers along ship track from the start of the microstructure survey and within isopycnals $24.8 < \sigma_\theta < 25.5$; red contour in Fig. 5), and

3) lateral mixing at the edges of the eddy ($s < 8 \, \text{km}$, $16 \, \text{km} < s < 27 \, \text{km}$, and $s > 35 \, \text{km}$, within isopycnals $23.6 < \sigma_\theta < 25$ and where the lateral thermal gradient magnitude is at least $5 \times 10^{-4} \, ^\circ\text{C m}^{-1}$; cyan contour in Fig. 5).

(i) Shear-driven turbulence beneath the eddy core

Density diffusivity due to shear-driven turbulence at the bottom of the eddy K_ρ^{bottom} is calculated using Osborn's 1980 equation, $K_\rho^{\text{bottom}} \leq \Gamma \langle \varepsilon \rangle / \langle N^2 \rangle$, in which Γ is a mixing efficiency and N^2 is the buoyancy frequency (Osborn 1980), and angled brackets indicate averages taken over all bins within the region. The Γ is generally taken to be 0.2 (e.g., Gregg et al. 2018). In fully developed turbulence, heat and density both diffuse at the same eddy diffusivity, and K_ρ^{bottom} is identical to the thermal diffusivity K_T^{bottom}. We assume this equivalence holds throughout the analysis.

Beneath the eddy's core, $\langle \varepsilon \rangle$ was $1.1 \times 10^{-9} \, \text{W kg}^{-1}$ and $\langle N^2 \rangle$ was $5.6 \times 10^{-4} \, \text{s}^{-1}$ [Figs. 9a(iii)–e(iii)]. This results in an upper bound for K_T^{bottom} of $4 \times 10^{-7} \, \text{m}^2 \, \text{s}^{-1}$ (about 2.5 times the molecular value for heat). The average T_z found beneath the eddy's core was $-0.3 \, ^\circ\text{C m}^{-1}$. The average heat flux $F_H^{\text{bottom}} = -\rho C_p K_T^{\text{bottom}} T_z$ out of the bottom of the eddy was estimated as $-0.5 \, \text{W m}^{-2}$ (Fig. 10c). The eddy's lifetime may be estimated by considering the integrated area flux of $4 \times 10^7 \, \text{W}$ removing the eddy's heat anomaly of $7 \times 10^{16} \, \text{J}$. This results in a decay time scale of 60 years.

(ii) Double-diffusive convection above the eddy core

Multiple methods have been used to estimate heat fluxes due to DDC. The Osborn–Cox equation, $K_T^{\text{OC}} = 0.5 \langle \chi \rangle / \langle \theta_z \rangle^2$ (Osborn and Cox 1972), in which angled brackets represent averaged values of χ and N^2 on isothermal surfaces, applies in the double-diffusive regime (see Winters and D'Asaro 1996). Care must be taken when calculating χ, which is generally determined via Fourier analysis over windows of approximately 1 m. Diffusive interfaces are much smaller than these windows, so a spectral window which includes an interface will give an erroneously high value for χ, due to contamination from the sharp change in background temperature gradient. It has been empirically demonstrated that the Osborn equation (Osborn 1980) also gives fairly reliable estimates for the effective diffusivity within diffusive layers provided that Γ is taken to be 1, rather than the conventional 0.2 (in a perfectly convecting cell, each convection cycle converts all kinetic energy to potential energy, and vice versa) (St. Laurent and Schmitt 1999; Inoue et al. 2007). Additionally, a variety of flux laws have been developed based on laboratory
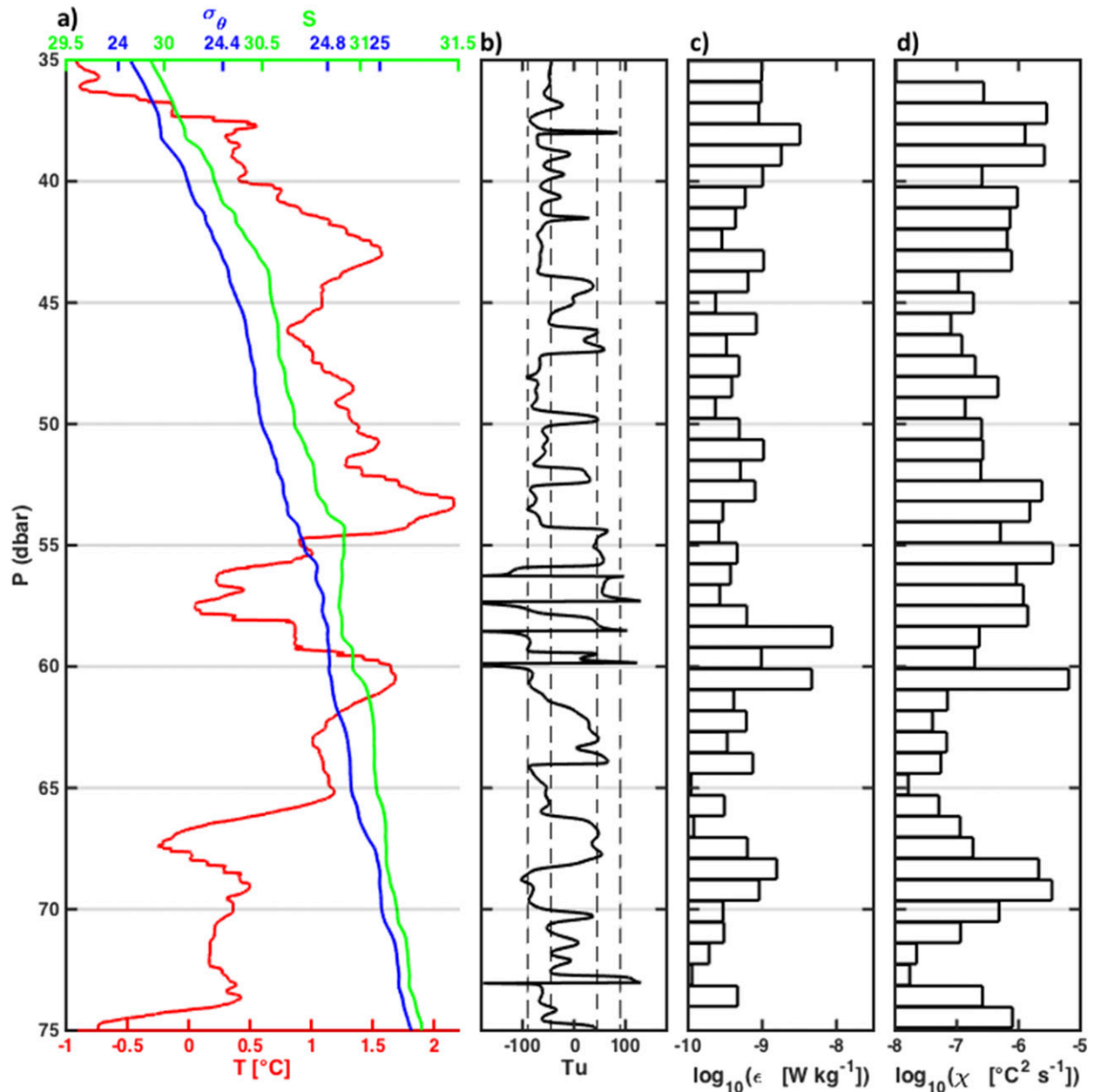
FIG. 8. A single profile in the intrusive region showing (a) high-resolution thermistor temperature and CTD salinity and density, (b) Turner angle, (c) ε, and (d) χ.

studies that relate heat flux to the temperature difference $\delta\theta$ across adjacent steps (e.g., Turner 1973; Kelley 1984, 1990; and others). These laws have the advantage that fluxes may be computed without microstructure measurements of temperature or shear. Such flux laws have been applied to oceanic DDC and appear to agree well with microstructure results (Padman and Dillon 1989; Sundfjord et al. 2007; Polyakov et al. 2012; Guthrie et al. 2015).

For the purpose of this analysis, four distinct methods were used to calculate the heat flux due to diffusive convection. First, for ease of comparison with the other processes, the Osborn–Cox equation was used with 0.25-m binned data with averages taken over the entire diffusive convective region (Fig. 9, top), so that flux derived from χ (F_χ) was estimated as $F_\chi = \rho C_p K_T^{OC} T_z$. In the region at the top of the eddy's core, $\langle\chi\rangle$ was $1.6 \times 10^{-6} (\degree C)^2\,s^{-1}$ and $\langle T_z\rangle$ was $1.0\degree C\,m^{-1}$. This method led
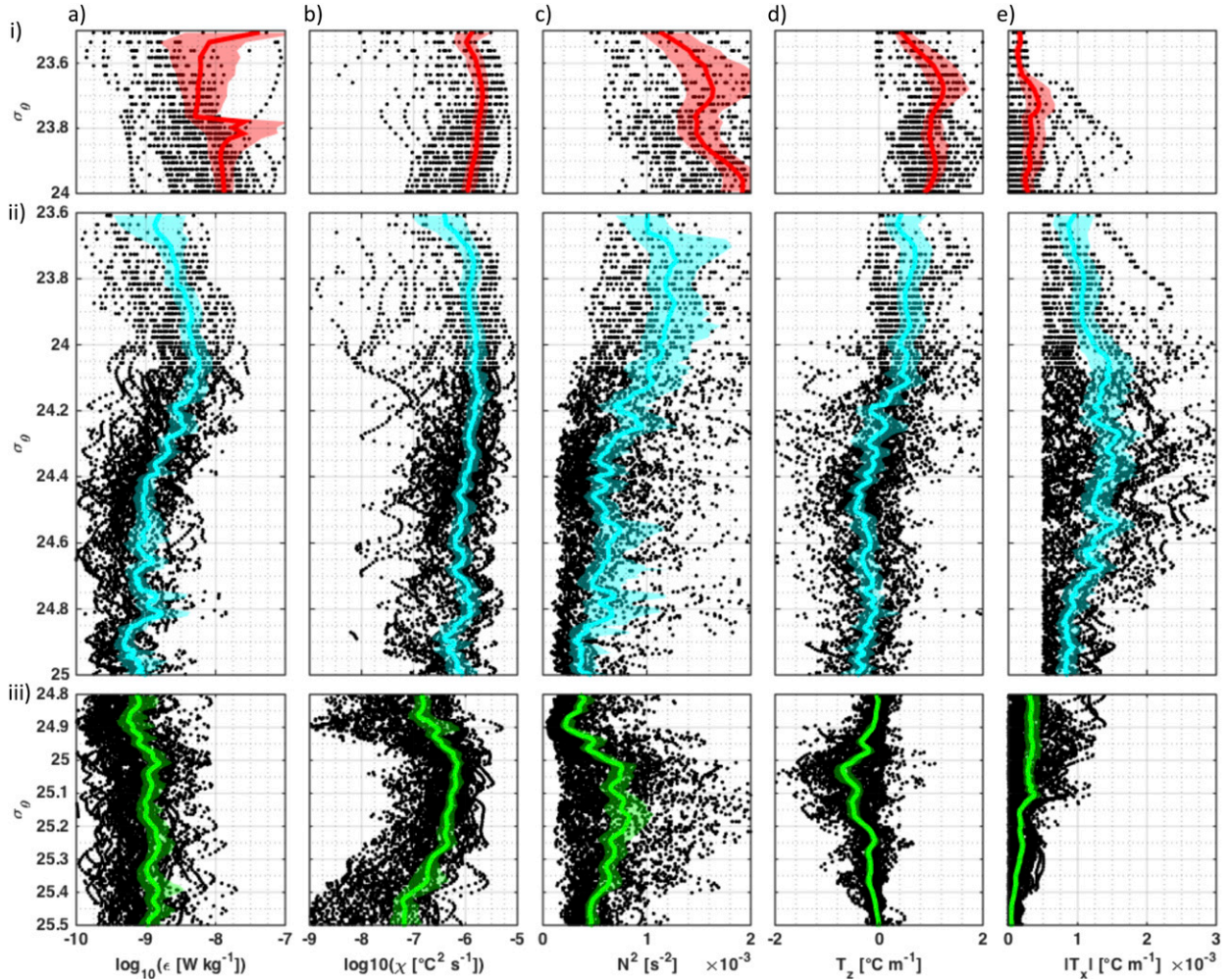
FIG. 9. Raw data and average profiles of (a) ε, (b) χ, (c) N^2, (d) $\partial T/\partial z$, and (e) $\overline{\partial T}/\partial x$ in boxes at the (i) top, (ii) sides, and (iii) bottom of the eddy. The lateral thermal gradient is never less than $5 \times 10^{-4}\,°\mathrm{C}\,\mathrm{m}^{-1}$ in the lateral region due to the definition of the lateral mixing region. Density ranges approximately correspond to 25–40 (top), 30–70 (sides), and 60–90 m (bottom). Bootstrapped 95% confidence intervals for each isopycnal bin are shaded. The lateral thermal gradient is smoothed laterally, so that results between profiles are correlated, reducing calculated sampling error.

to an effective diffusivity K_T^{OC} of $8 \times 10^{-7}\,\mathrm{m}^2\,\mathrm{s}^{-1}$ and an estimated heat flux of $3\,\mathrm{W}\,\mathrm{m}^{-2}$.

For a more robust analysis, we followed the methods of Padman and Dillon (1989), who calculated diffusive convective fluxes within each layer of a diffusive staircase (see Fig. 11). In this analysis, windows containing only the well-mixed diffusive layers were hand-selected for each profile. While these fluxes should ideally be calculated based on values averaged horizontally along a single diffusive layer, we found it difficult to trace single layers over multiple adjacent profiles, likely due to the short height of layers and the high-shear background environment that may result in intermittent disruptions to layers. For this reason, fluxes were calculated from values determined within each layer for each profile.

The reported results are an average of such fluxes. Both the Osborn–Cox and the Osborn equation with $\Gamma = 1$ were used to calculate fluxes within each layer. The calculated fluxes over the diffusive convective region were $6\,\mathrm{W}\,\mathrm{m}^{-2}$, using $F_{\chi_{\mathrm{layers}}} = \rho C_p K_{T_{\mathrm{layers}}}^{\mathrm{OC}} T_z$, and $4\,\mathrm{W}\,\mathrm{m}^{-2}$, using $F_{\varepsilon_{\mathrm{layers}}} = \rho C_p K_{T_{\mathrm{layers}}}^{O} T_z$, in which $K_{T_{\mathrm{layers}}}^{O}$ was calculated with $\Gamma = 1$.

Because empirical flux laws are frequently used when microstructure measurements are not available, we also compared these results to those found using the flux law described by Kelley (1990) and verified by Guthrie et al. (2015):

$$F_{4/3} = 0.0032 \exp\left(\frac{4.8}{R_\rho^{0.72}}\right)\rho C_p \left(\frac{\alpha g \kappa}{P_r}\right)^{1/3}\delta\theta^{4/3}, \quad (2)$$
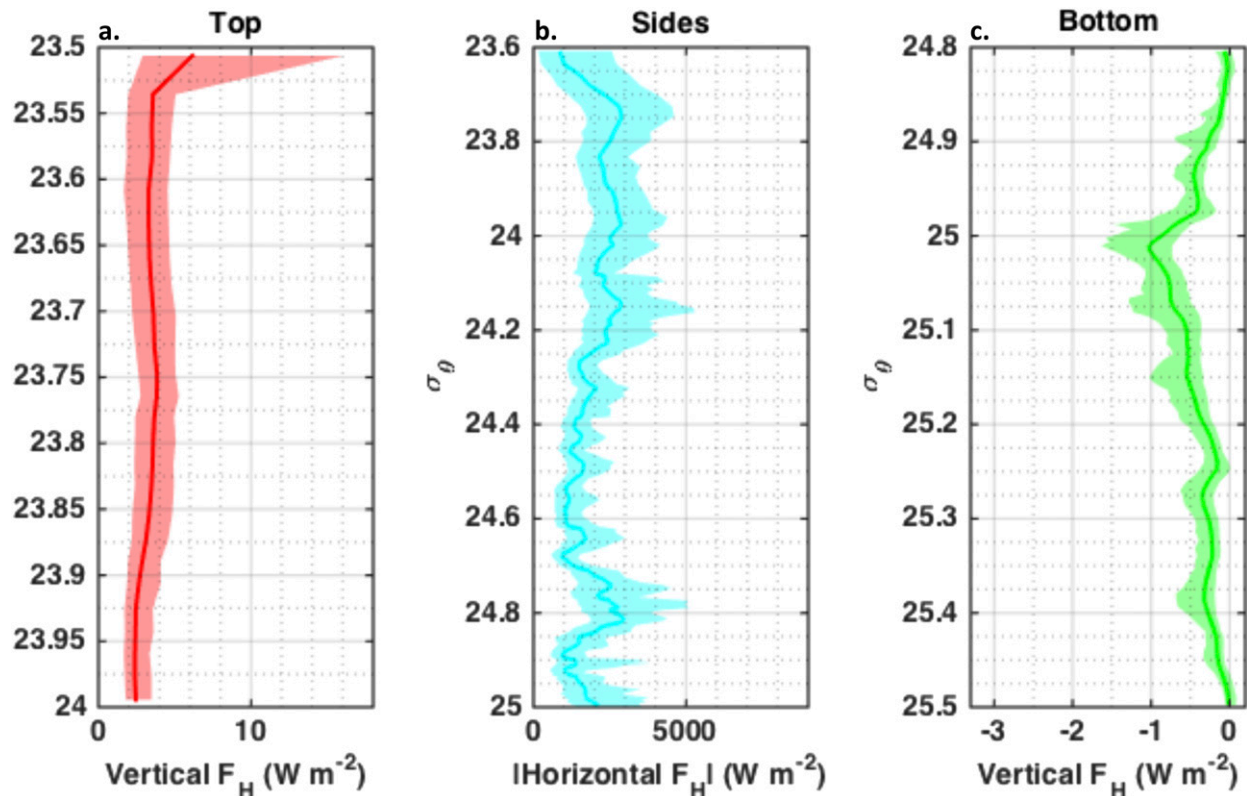
FIG. 10. Heat fluxes calculated from averaged quantities shown in Fig. 9 for the (a) top, (b) sides, and (c) bottom edges of the eddy. Density ranges approximately correspond to 25–40 (top), 30–70 (sides), and 60–90 m (bottom). Bootstrapped 95% confidence intervals are shaded; note that these intervals are generally within the factor of 2–3 uncertainty associated with measurements of ε and χ.

In Eq. (2), R_ρ is the density ratio as defined above and averaged over a profile, $\rho = 1025\,\text{kg}\,\text{m}^{-3}$ is density, $C_p = 4000\,\text{J}\,\text{K}^{-1}\,\text{kg}^{-1}$ is the heat capacity of saltwater, $\kappa = 1.4 \times 10^{-7}\,\text{m}^2\,\text{s}^{-1}$ is the molecular diffusivity of heat, $P_r = \nu/\kappa$ is the dimensionless Prandtl number (with the kinematic viscosity $\nu = 1.8 \times 10^{-6}\,\text{m}^2\,\text{s}^{-1}$), and $\delta\theta$ is the difference in potential temperature between adjacent layers. In general, $F_{4/3}$ is higher than that derived from both F_{χ_layers} and $F_{\varepsilon_\text{layers}}$, with an average value of $12\,\text{W}\,\text{m}^{-2}$.

Although agreement between all methods is fair, the two estimates of flux derived from χ and ε within layers (F_{χ_layers} and $F_{\varepsilon_\text{layers}}$) incorporate all available information (both the microstructure data and the boundaries of layers), and we suspect these are the most accurate methods. Averaging these estimates together, the total heat flux over the top of the eddy core is an estimated $F_H^\text{top} = 5\,\text{W}\,\text{m}^{-2}$. With a vertical temperature gradient of $1.0°\text{C}\,\text{m}^{-1}$, this corresponds to an approximate thermal diffusivity K_T^top of $1.2 \times 10^{-6}\,\text{m}^2\,\text{s}^{-1}$. Taking the area-integrated heat flux as $4 \times 10^8\,\text{W}$ and the eddy's heat anomaly of $7 \times 10^{16}\,\text{J}$ suggests a decay time scale of 6 years.

(iii) Lateral intrusions on the sides of the eddy

Assuming that the intrusions are in approximate steady state, all vertical production of temperature variance must be balanced by large-scale horizontal production of variance. The effective isopycnal thermal diffusivity due to advection along intrusions $K_{T_I}^\text{sides}$ can be calculated from diapycnal diffusivity $K_{T_D}^\text{sides}$ as $K_{T_I}^\text{sides} = \overline{K_{T_D}^\text{sides} T_z^2}/\overline{T_x}^2$ (Ruddick et al. 2010), in which $\overline{T_x}$ represents the bulk lateral gradient and $\overline{K_{T_D}^\text{sides} T_z^2}$ is averaged over the entire intrusive region. Ruddick et al. (2010) obtained this result by equating the horizontal production of thermal gradient variance to the vertical production averaged over all the intrusive surfaces, which is in turn equated to the average χ.

The simplest way to calculate $K_{T_D}^\text{sides}$ within the intrusive region is by taking the Osborn–Cox equation $K_{T_D}^\text{sides} = 0.5\langle\chi\rangle/\langle\theta_z\rangle^2$ and using this to calculate $K_{T_I}^\text{sides}$ from the averaged χ and T_x within the intrusive region. We found $\langle\chi\rangle$ in this region was $1.09 \times 10^{-6}(°\text{C})^2\,\text{s}^{-1}$ and $\langle T_x\rangle$ was $1.2 \times 10^{-3}°\text{C}\,\text{m}^{-1}$ (Fig. 9). This results in an estimated $K_{T_I}^\text{sides}$ of $0.4\,\text{m}^2\,\text{s}^{-1}$. The lateral heat flux F_H^sides is $2000\,\text{W}\,\text{m}^{-2}$ (Fig. 10), and the corresponding
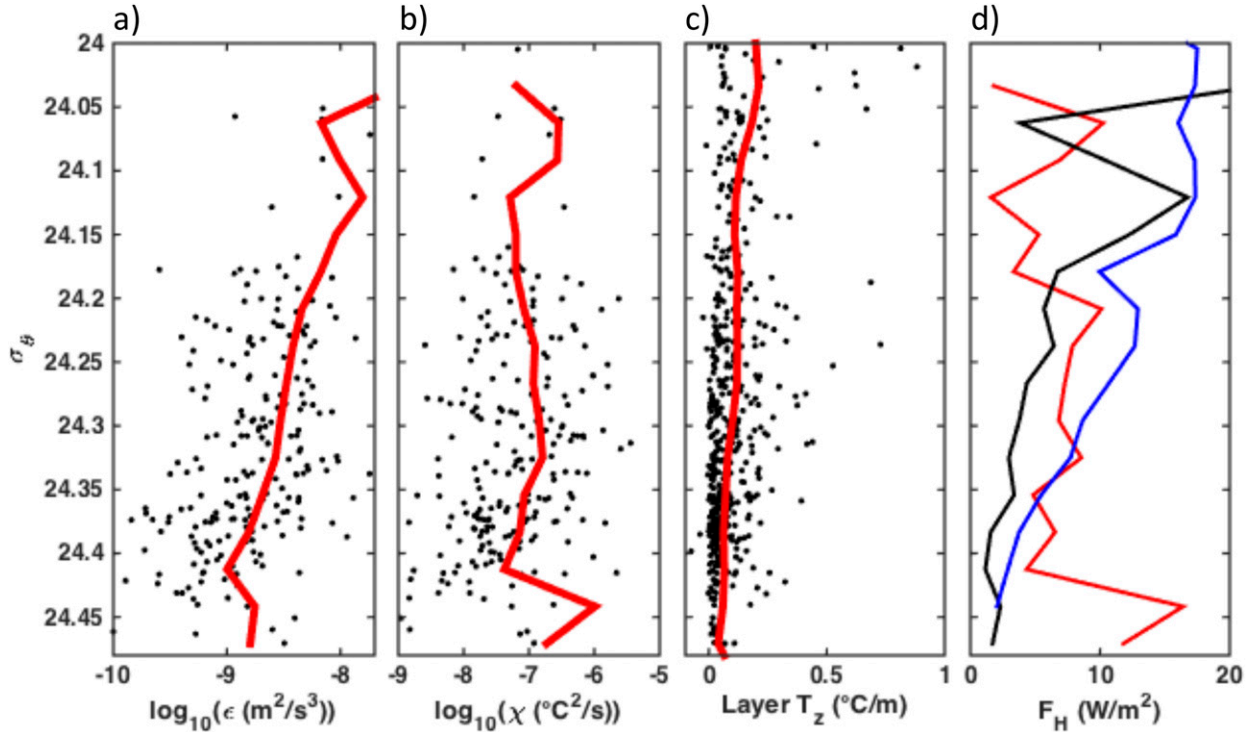
FIG. 11. Quantities averaged within diffusive layers at the top of the eddy: (a) ε calculated within layers, (b) χ calculated within layers, (c) $\partial T/\partial z$ within layers (used along with ε and χ within layers to calculate heat fluxes within each layer), (d) F_ε (black), F_χ (red), and $F_{4/3}$ (blue).

lifetime taking area-integrated heat flux of 2×10^9 W and assuming this removes the eddy's heat anomaly of 7×10^{16} J suggests a decay time scale of 1 year.

Within the intrusive region, accurately calculating χ is somewhat challenging as intrusions can occur on very small scales and are difficult to distinguish from turbulent features (see appendix). Therefore, we additionally use measured ε to bound the lateral flux as follows.

There are two distinct processes that can result in elevated ε: 1) shear-driven turbulent mixing can occur along intrusions, either as the large-scale azimuthal velocity of the eddy is converted to intrusion-scale shear or due to other sources of shear, and 2) DDC can occur above warm/salty intrusions. While characteristic diffusive layers are apparent above intrusions in some profiles, these are not coherent across multiple profiles, suggesting that there is sufficient shear to disrupt DDC cells and that both DDC and shear-driven turbulence could contribute to the observed ε. We treat the two extreme cases of pure shear-driven turbulence and pure DDC using Osborn's equation $K_{T_D}^{\text{sides}} = \Gamma \langle \varepsilon \rangle / \langle N^2 \rangle$. For shear-driven turbulence, the mixing efficiency Γ is set to 0.2, while for DDC Γ can be taken to be 1 (St. Laurent and Schmitt 1999; Inoue et al. 2007). Thus, assuming that the observed ε is entirely due to shear-driven turbulence

(DDC) results in a lower (upper) bound on the effective lateral diffusivity and resulting heat flux.

To bound heat flux, we set $K_{T_D}^{\text{sides}} = \Gamma \langle \varepsilon \rangle / \langle N^2 \rangle$ and proceed to calculate $K_{T_I}^{\text{sides}} = K_{T_D}^{\text{sides}} \langle T_z^2 \rangle / \langle T_x \rangle^2$. With $\langle \varepsilon \rangle = 2.0 \times 10^{-9}$ W kg^{-1}, $\langle N^2 \rangle = 7.1 \times 10^{-4}$ s^{-2}, $\langle |T_x| \rangle = 1.2 \times 10^{-3}$°C m^{-1}, and $\langle T_z^2 \rangle = 0.44$(°C)^2 m^{-2}, the resulting bounds on $K_{T_I}^{\text{sides}}$ are 0.2–0.8 m^2 s^{-1} (for Γ in the range of 0.2–1; Fig. 9). The corresponding range of heat flux is 800–4000 W m^{-2}.

Both upper and lower bounds are within a factor of 3 of the original estimate of $F_H^{\text{sides}} = 2000$ W m^{-2} from χ and are thus within the instrument error associated with measurements of χ and ε. Although we lack the horizontal resolution to fully verify the Ruddick et al. (2010) method for calculating $K_{T_I}^{\text{sides}}$, we can use the assertion that the total vertical transport of heat out of the eddy along intrusions must be balanced by an advective flux along intrusions to assess whether the model is physically realistic. Considering the average vertical heat flux in the intrusive region, $\rho C p K_{T_D}^{\text{sides}} |T_z| = 3$ W m^{-2} and the horizontal heat flux $\rho C p K_{T_I}^{\text{sides}} |T_x| = 2000$ W m^{-2}, we see that these differ by a factor of 700. The net heat transport through the vertical surfaces above and below isopycnals must match the horizontal heat transport. Assuming that both lateral and vertical heat fluxes occur over the same
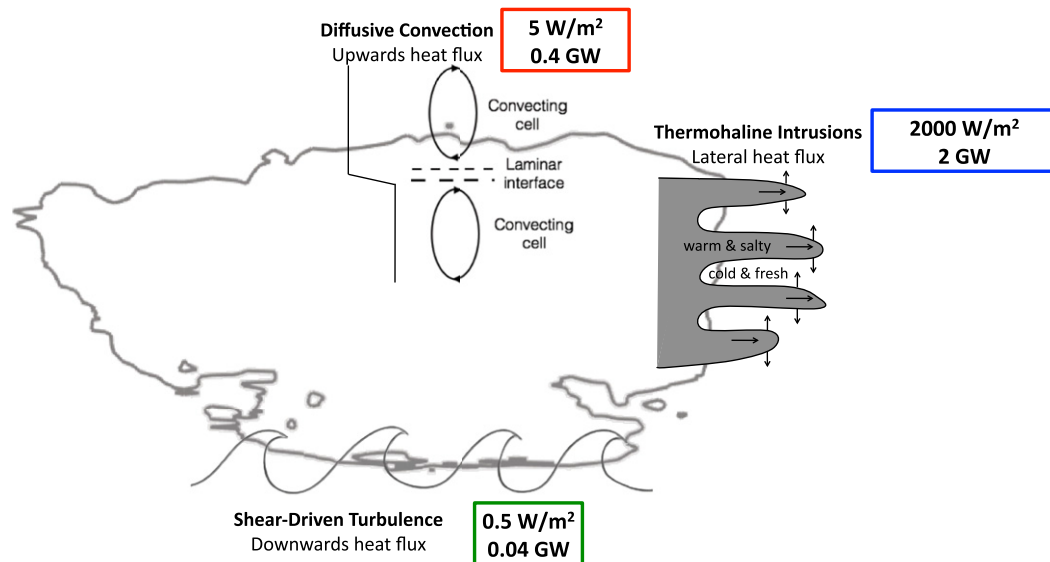
FIG. 12. Schematic diagram of the eddy, indicating diffusive convection at its top, lateral intrusions at its sides, and shear-driven turbulence at its bottom. Estimated heat fluxes and transports due to each process are noted.

radial distance, this factor of 700 must represent the ratio of the vertical height of the eddy core (corresponding to the distance over which lateral heat flux occurs) to the pathlength along intrusions (corresponding to the distance over which the vertical heat flux occurs). Taking the height of the intrusive region to be 30 m, this implies an along-intrusion pathlength of 20 km. The intrusive region extends about 2–3 km. Individual intrusions extend up to 2 km so that a total pathlength of 20 km due to four or five intrusions is plausible.

4. Total heat loss implications

Putting together the results of the last section, a picture emerges of a warm eddy losing heat from its top, bottom, and sides (Fig. 12). Using the results from the last section and modeling the eddy as a cylinder with a height of 40 m and a radius of 5 km, we can calculate the total heat transport out of the eddy due to each of the identified processes: 1) shear-driven turbulence acting at the bottom of the eddy transports 0.04 GW (from 0.01 to 0.1 GW), 2) DDC acting at the top of the eddy transports 0.5 GW (from 0.2 to 1.5 GW), and 3) lateral intrusions acting along the sides of the eddy transport 2 GW (from 1 to 6 GW). Our measurements show a net heat flux out of the eddy at this time of 2.5 GW; if this were simplistically extrapolated into the future it suggests a decay time scale of about a year. Complete results are given in Table 3.

5. Summary and discussion

The structure and dynamics of a warm-core intra-halocline anticyclonic eddy observed on the Chukchi shelf in September of 2015 have been described. With core temperatures around 6°C, this eddy was extremely warm compared to most prior observations of Arctic eddies, although the eddy described by Kawaguchi et al. (2012) was similarly warm. A 6°C intrusion was also observed in the Canada Basin at approximately 50-m depth by an ice-tethered-profiler in 2010 (Timmermans and Jayne 2016). The recent appearance of these warm sub-surface features suggests that either modern sampling schemes are capturing intermittent features that were previously unobserved or that temperature anomalies of 6°C in the western Arctic are a relatively new phenomenon. Such structures may play an important role in the transport of Pacific-origin heat and freshwater in the Canada Basin and may have biological effects as well.

Microstructure measurements through the eddy core determined that while ε was generally weak beneath the mixed layer, ε was elevated surrounding the eddy core $\left[\mathcal{O}(10^{-8})\,\mathrm{W\,kg^{-1}}\right]$ as a result of three different processes: shear-driven overturns below the eddy core, diffusive convection above the core, and lateral mixing due to intrusions along the sides of the eddy. The eddy lost heat at a rate of 2.5 GW, with lateral mixing responsible for approximately 80% of this heat loss and DDC accounting for the remaining 20%. Heat loss by shear turbulence at the bottom of the eddy was negligible.

These estimates are subject to many sources of error. Inferring ε and χ from microstructure shear and temperature measurements is subject to errors of up to a factor of 3. Our windowing procedure for calculating χ (appendix) is subjective and subject to error, particularly in intrusive regions as distinguishing between turbulent

TABLE 3. Heat fluxes, areas, transports, diffusivity, and estimated lifetimes for each edge of the eddy core. Error bounds are given for heat flux based on the spread of alternate methods for calculating heat flux [section 3b(2)]; only one method was used to calculate heat flux out of the bottom of the eddy, so quantitative error bounds cannot be determined as systemic error is likely much larger than sampling error (Fig. 10). Errors in the range of factors of 2–3 are frequently associated with this type of turbulence measurement (Peters et al. 1988).

Region	Flux (W m^{-2})	Area (m^2)	Transport (GW)	K (m^2 s^{-1})	Lifetime (yr)
Above eddy core	5 (3, 12)	8×10^7	0.4	3×10^{-6}	6
Eddy flanks	2000 (800, 4000)	1×10^6	2	0.4	1
Beneath eddy core	-0.5	8×10^7	-0.04	4×10^{-7}	60

mixing and small-scale thermohaline intrusions is extremely difficult. The validity of the Ruddick et al. (2010) formulation for the decay of an eddy to thermohaline intrusions has not been established outside of the meddy Sharon; in the Arctic Ocean the thermal expansion coefficient α is quite small and varies strongly with temperature, which may affect the results. Additionally, we assume the turbulence is isotropic even though this is a low shear environment in which this assumption may not hold at all times. We use canonical values for Γ of 0.2 in shear-driven turbulence and 1 in DDC turbulence although the accuracy of these values is an area of active research. We have also extrapolated heat fluxes for the entire eddy based on a pair of transects, neither of which bisected the eddy's center. However, the lifetime we estimate for the eddy of approximately a year is in line both with other observations of small Arctic eddies (e.g., D'Asaro 1988a; Zhao et al. 2014) and with the observed decay of the meddy Sharon, which also decayed as a result of thermohaline intrusions (Armi et al. 1989; Ruddick et al. 2010).

The 5 W m^{-2} DDC flux present above the eddy is notable in contrast to the relatively weak effect of the ubiquitous diffusive layers at the top of the Atlantic Water, which are thought to be associated with maximal heat fluxes of 0.3 W m^{-2} in the Canada Basin (Timmermans et al. 2008a). The larger DDC fluxes observed above the eddy are more similar in magnitude to those observed in the Eurasian Basin (Padman and Dillon 1991; Polyakov et al. 2012) and occur because of the significant temperature gradient $[\mathscr{O}(1)°\text{C m}^{-1}]$ and unstable density ratio above the eddy. The relatively high-shear environment may also play a role in increasing fluxes through the diffusive staircase as the ambient shear injects energy and creates instabilities between the convecting cells and interfaces that separate them (Padman 1994; Stamp et al. 1998; Smyth and Kimura 2007). The fluxes calculated in the above analysis are lower than the average fluxes of 20 W m^{-2} that Kawaguchi et al. (2012) observed above a similar warm-core eddy. This may be partially explained because Kawaguchi et al. (2012) observed extremely elevated

values of χ in a few regions, which they attributed to intense double-diffusive mixing. However, their very high χ values may also be overestimates that result from taking spectral windows over the discrete steps within a DDC staircase; such steps contaminate the Fourier transform at all scales and are inconsistent with the turbulence theory underlying this analysis technique (see appendix for details).

Existing literature suggests eddies are generated both in Barrow Canyon and along the Beaufort and Chukchi shelf breaks (D'Asaro 1988a; Pickart et al. 2005; Spall et al. 2008). While most studies have focused on cold-core eddies, eddies such as the one described in this study could play an important role in transporting warm coastal water into the interior of the Arctic basin. We estimate the observed eddy has a lifetime of ~1 year; assuming it continued to travel at a rate of 8 cm s^{-1} into the basin, this would allow it to penetrate ~1500 km into the basin, carrying heat, salt, and nutrients with it. However, this assumes that the eddy dynamics remain constant in time, which may not be the case. During the fall and winter as the mixed layer deepens, shear-driven mixing may play an increasingly important role in extracting heat from the eddy. Profiles collected in the Beaufort Sea of October 2015 in similar regions suggest the mixed layer can deepen to 25 or 30 m as early as October (Toole et al. 2010; Timmermans 2015; Smith et al. 2018). If the eddy were to persist at the same depth into the autumn and encountered such conditions, its dynamics would rapidly change, likely resulting in its dissolution and the release of its heat to the mixed layer. Assuming the eddy survived 40 days after observation and continued to drift at 8 cm s^{-1}, it would penetrate about 300 km into the Canada Basin during this timeframe.

Brugler et al. (2014) suggest that summer heat transport in the Alaskan Coastal Current (ACC) at the base of Barrow Canyon averages around 3 TW, while Corlett and Pickart (2017) estimate 1.4 TW of heat are advected west along the Chukchi slope in a baroclinically unstable current (known as the Chukchi Slope Current) from July to October. These pathways account for approximately

3×10^{19} J of heat each year. The ultimate fate of this heat is unclear. Some of it is likely lost to the atmosphere, some may be used to melt local sea ice, and some makes its way into the Canada Basin, where it persists as a year-round subsurface temperature maximum. If all of the heat were dispersed into the basin in eddies like the one described in this study, this would correspond to the formation of ~400 eddies each year. However, most PSW is not contained in such eddies but is distributed throughout the Beaufort Sea in interleaving filaments and intrusions (e.g., Timmermans et al. 2014; Kawaguchi et al. 2014; Timmermans and Jayne 2016). Such structures may also be susceptible to processes that mix heat both vertically and laterally, but the net heat fluxes and the relative importance of each process may be quite different.

Thermohaline intrusions may act directly on currents carrying ACW. If thermohaline intrusions similar to those along the eddy flanks exist along both the Beaufort shelfbreak jet and the Chukchi Slope Current, the total distance susceptible to intrusions would be 1300 km. Assuming a current depth of 50 m for both currents gives a total surface area of $6.5 \times 10^7 \, \text{m}^2$ facing into the basin for these currents. A lateral flux of $2000 \, \text{W m}^{-2}$ along this area would result in a total lateral heat transport of 0.2 TW. This is another pathway that could allow heat to enter the Canada Basin from these topographically trapped currents.

Within a rapidly changing Arctic, oceanic heat may play a crucial role in the growth–melt cycle of sea ice and in setting local stratification. Improving our understanding of the pathways heat takes into the basin interior and the processes that drive both vertical and lateral oceanic heat fluxes are necessary steps toward developing better models of the Arctic climate. Warm-core eddies may represent an important pathway for Pacific-origin heat into the central basin. However, the frequency of formation of such eddies and their response to seasonal deepening of the mixed layer is unknown at this time, and many questions remain to be answered.

APPENDIX

χ in Double-Diffusive Environments

The χ is usually understood in the context of Osborn–Cox-style analysis, in which the small-scale variance of the thermal gradient is used to estimate thermal diffusivity. In using maximum-likelihood estimation to fit Batchelor spectra to the spectra of microstructure measurements of the thermal gradients, 1- to 2-m windows are generally used. When this spectral analysis is used to infer thermal diffusivity, there is an implicit assumption that the background thermal gradient varies slowly over such length scales, so that the spectra of thermal variance relate directly to the microscale mixing associated with fully developed isotropic turbulence.

In the Arctic Ocean, the temperature gradient at length scales of 1–2 m can vary rapidly in the presence of diffusive layers or thermohaline intrusions, as shown in Fig. A1 (see also, e.g., Guthrie et al. 2015). If spectra are calculated over windows that span such larger-scale variation, the high-wavenumber portion of the temperature gradient will consist of both small temperature anomalies that relate to thermal diffusivity in a traditional Osborn–Cox sense and of the high-wavenumber signatures of larger-scale intrusions or diffusive steps. When double-diffusive interfaces or intrusions occur on length scales similar to those seen in isotropic turbulence, this leads to overestimation of the thermal diffusivity and heat flux calculated from χ, since the measured high-wavenumber thermal variance is only partially due to microscale mixing. Spectra taken over such windows deviate from a Batchelor curve as a spike in the thermal gradient contaminates all wavenumbers longer than the width of the spike in spectral space.

In general, when spectra deviate too far from a Batchelor spectra the MLE analysis will not converge in a given window. In windows where this occurred, microstructure temperature was examined by eye. When possible, the window was broken down into regions in which the background thermal gradient varied slowly, and the bin estimate for χ was computed as a weighted average of these subbinned values. Figure A1
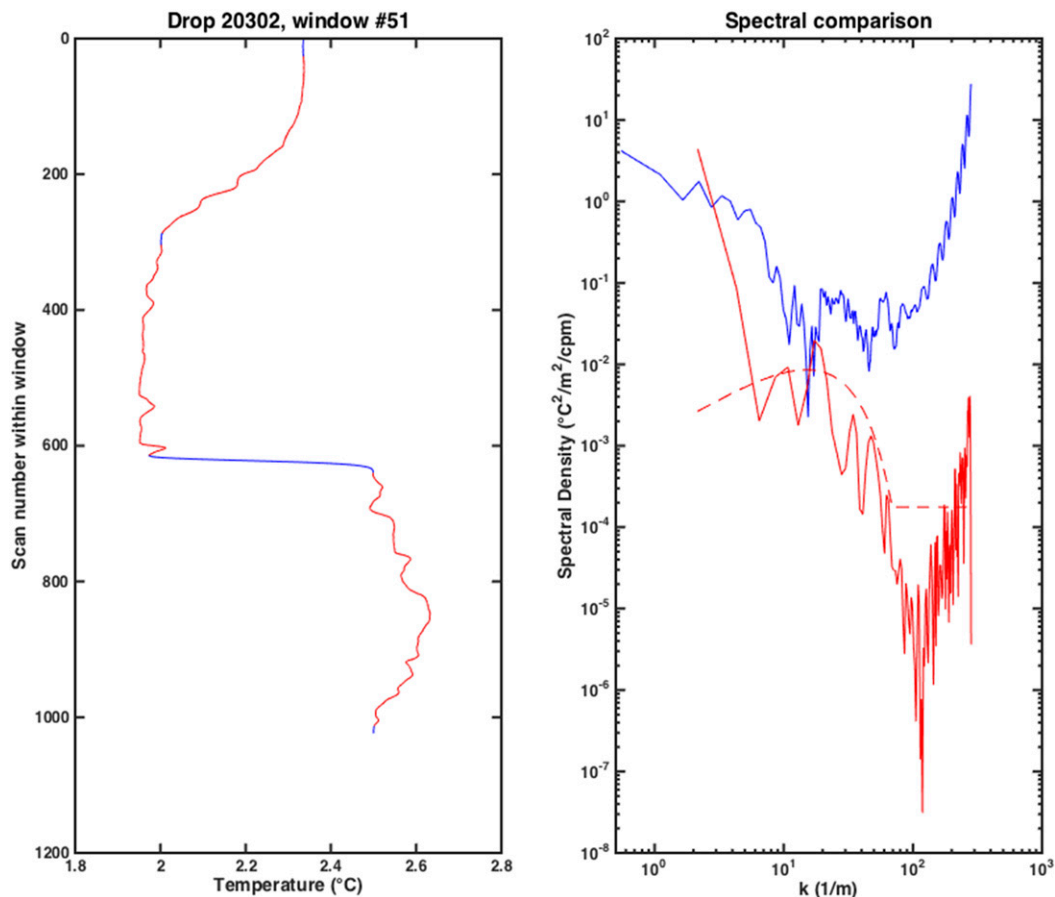
FIG. A1. Example window in which estimates of χ did not converge owing to the sharp step within the sampled window. (left) The thermistor temperature over the full window (blue), while the red sections represent the region in which χ was recalculated using handpicked windows. (right) The original spectrum (blue) and the spectrum taken over the upper subwindow (red) are shown, along with the MLE fit to the latter (red, dashed). The MLE method does not converge for the spectrum taken over the entire original window. Integrating under the spectrum over the full original window results in an estimate for χ that is two orders of magnitude higher than that obtained by taking the weighted average of the hand selected windows.

shows one such window, the spectra calculated over this window, and the subwindows that were used for the final gridded χ product as well as the spectra for a representative subwindow. While the MLE analysis would not converge over the original window, simply summing the variance beneath a cutoff wavenumber gives an estimated χ of $4 \times 10^{-4} (°C)^2 \, s^{-1}$. Taking a weighted average over the MLE estimates within each subwindow produces $5 \times 10^{-7} (°C)^2 \, s^{-1}$ for the gridded χ value for this window. In this case there is a factor of 1000 difference between simple integration of the spectrum of thermal variance and careful MLE fitting within hand-selected subwindows.

This method is subject to some uncertainties. The MLE estimate may converge in windows that include some variation of background χ that is not due to turbulent mixing, biasing estimates high. We lack a rigorous method

to distinguish between small-scale thermal variations due to mixing versus those due to small-scale interleaving. For this reason, all estimates of physical quantities based on measured χ are compared to estimates based on measured ε; generally these two methods show good agreement.

REFERENCES

Armi, L., and W. Zenk, 1984: Large lenses of highly saline Mediterranean water. *J. Phys. Oceanogr.*, **14**, 1560–1576, https://doi.org/10.1175/1520-0485(1984)014<1560:LLOHSM>2.0.CO;2.

——, D. Hebert, N. Oakey, J. Price, P. Richardson, H. T. Rossby, and B. Ruddick, 1989: Two years in the life of a Mediterranean salt lens. *J. Phys. Oceanogr.*, **19**, 354–370, https://doi.org/10.1175/1520-0485(1989)019<0354:TYITLO>2.0.CO;2.

Bebieva, Y., and M.-L. Timmermans, 2015: An examination of double-diffusive processes in a mesoscale eddy in the Arctic Ocean. *J. Geophys. Res. Oceans*, **121**, 457–475, https://doi.org/10.1002/2015JC011105.

——, and ——, 2017: The relationship between double-diffusive intrusions and staircases in the Arctic Ocean. *J. Phys. Oceanogr.*, **47**, 867–878, https://doi.org/10.1175/JPO-D-16-0265.1.

Brugler, E. T., R. S. Pickart, G. W. K. Moore, S. Roberts, T. Weingartner, and H. Statscewich, 2014: Seasonal to interannual variability of the Pacific water boundary current in the Beaufort Sea. *Prog. Oceanogr.*, **127**, 1–20, https://doi.org/10.1016/j.pocean.2014.05.002.

Carmack, E., and Coauthors, 2015: Toward quantifying the increasing role of oceanic heat in sea ice loss in the new Arctic. *Bull. Amer. Meteor. Soc.*, **96**, 2079–2105, https://doi.org/10.1175/BAMS-D-13-00177.1.

Chao, S.-Y., and P.-T. Shaw, 2003: A numerical study of dense water outflows and halocline anticyclones in an Arctic baroclinic slope current. *J. Geophys. Res.*, **108**, 3226, https://doi.org/10.1029/2002JC001473.

Corlett, W. B., and R. S. Pickart, 2017: The Chukchi slope current. *Prog. Oceanogr.*, **153**, 50–65, https://doi.org/10.1016/j.pocean.2017.04.005.

D'Asaro, E. A., 1988a: Generation of submesoscale vortices: A new mechanism. *J. Geophys. Res.*, **93**, 6685–6693, https://doi.org/10.1029/JC093iC06p06685.

——, 1988b: Observations of small eddies in the Beaufort Sea. *J. Geophys. Res.*, **93**, 6669–6684, https://doi.org/10.1029/JC093iC06p06669.

——, and M. D. Morehead, 1991: Internal waves and velocity fine structure in the Arctic Ocean. *J. Geophys. Res.*, **96**, 12 725–12 738, https://doi.org/10.1029/91JC01071.

——, and J. H. Morison, 1992: Internal waves and mixing in the Arctic Ocean. *Deep-Sea Res.*, **39** (Suppl.), S459–S484, https://doi.org/10.1016/S0198-0149(06)80016-6.

Eisenman, I., T. Schneider, D. S. Battisti, and C. M. Bitz, 2011: Consistent changes in the sea ice seasonal cycle in response to global warming. *J. Climate*, **24**, 5325–5335, https://doi.org/10.1175/2011JCLI4051.1.

Fer, I., 2009: Weak vertical diffusion allows maintenance of cold halocline in the central Arctic. *Atmos. Oceanic Sci. Lett.*, **2**, 148–152, https://doi.org/10.1080/16742834.2009.11446789.

——, R. Skogseth, and F. Geyer, 2010: Internal waves and mixing in the marginal ice zone near the Yermak Plateau. *J. Phys. Oceanogr.*, **40**, 1613–1630, https://doi.org/10.1175/2010JPO4371.1.

Gregg, M. C., 1980: Microstructure patches in the thermocline. *J. Phys. Oceanogr.*, **10**, 915–943, https://doi.org/10.1175/1520-0485(1980)010<0915:MPITT>2.0.CO;2.

——, and L. J. Pratt, 2010: Flow and hydraulics near the sill of Hood Canal, a strongly sheared, continuously stratified fjord. *J. Phys. Oceanogr.*, **40**, 1087–1105, https://doi.org/10.1175/2010JPO4312.1.

——, D. Winkel, and T. Sanford, 1993: Varieties of fully resolved spectra of vertical shear. *J. Phys. Oceanogr.*, **23**, 124–141, https://doi.org/10.1175/1520-0485(1993)023<0124:VOFRSO>2.0.CO;2.

——, E. D'Asaro, J. Riley, and E. Kunze, 2018: Mixing efficiency in the ocean. *Annu. Rev. Mar. Sci.*, **10**, 443–473, https://doi.org/10.1146/annurev-marine-121916-063643.

Guthrie, J. D., I. Fer, and J. Morison, 2015: Observational validation of the diffusive convection flux laws in the Amundsen Basin, Arctic Ocean. *J. Geophys. Res. Oceans*, **120**, 7880–7896, https://doi.org/10.1002/2015JC010884.

Halle, C., 2003: Internal wave variability in the Beaufort Sea during the winter of 1993/1994. *J. Geophys. Res.*, **108**, 3210, https://doi.org/10.1029/2000JC000703.

Hunkins, K. L., 1974: Subsurface eddies in the Arctic Ocean. *Deep-Sea Res. Oceanogr. Abstr.*, **21**, 1017–1033, https://doi.org/10.1016/0011-7471(74)90064-3.

Huppert, H. E., and J. S. Turner, 1981: Double-diffusive convection. *J. Fluid Mech.*, **106**, 299–329, https://doi.org/10.1017/S0022112081001614.

Inoue, R., H. Yamazaki, F. Wolk, T. Kono, and J. Yoshida, 2007: An estimation of buoyancy flux for a mixture of turbulence and double diffusion. *J. Phys. Oceanogr.*, **37**, 611–624, https://doi.org/10.1175/JPO2996.1.

Kadko, D., R. S. Pickart, and J. Mathis, 2008: Age characteristics of a shelf-break eddy in the western Arctic and implications for shelf-basin exchange. *J. Geophys. Res.*, **113**, C02018, https://doi.org/10.1029/2007JC004429.

Kawaguchi, Y., M. Itoh, and S. Nishino, 2012: Detailed survey of a large baroclinic eddy with extremely high temperatures in the western Canada Basin. *Deep-Sea Res. I*, **66**, 90–102, https://doi.org/10.1016/j.dsr.2012.04.006.

——, T. Kikuchi, and R. Inoue, 2014: Vertical heat transfer based on direct microstructure measurements in the ice-free Pacific-side Arctic Ocean: The role and impact of the Pacific water intrusion. *J. Oceanogr.*, **70**, 343–353, https://doi.org/10.1007/s10872-014-0234-8.

——, S. Nishino, J. Inoue, K. Maeno, H. Takeda, and K. Oshima, 2016: Enhanced diapycnal mixing due to near-inertial internal waves propagating through an anticyclonic eddy in the ice-free Chukchi Plateau. *J. Phys. Oceanogr.*, **46**, 2457–2481, https://doi.org/10.1175/JPO-D-15-0150.1.

Kelley, D. E., 1984: Effective diffusivities within oceanic thermohaline staircases. *J. Geophys. Res.*, **89**, 10 484–10 488, https://doi.org/10.1029/JC089iC06p10484.

——, 1990: Fluxes through diffusive staircases, a new formulation. *J. Geophys. Res.*, **95**, 3365–3371, https://doi.org/10.1029/JC095iC03p03365.

——, H. J. S. Fernando, A. E. Gargett, J. Tanny, and E. Özsoy, 2003: The diffusive regime of double-diffusive convection. *Prog. Oceanogr.*, **56**, 461–481, https://doi.org/10.1016/S0079-6611(03)00026-0.

Krishfield, R. A., A. J. Plueddemann, and S. Honjo, 2002: Eddys in the Arctic Ocean from IOEB ADCP data. Woods Hole Oceanographic Institution Tech. Rep. WHOI-2002-09, 151 pp., https://doi.org/10.1575/1912/30.

Kunze, E., 1985: Near-inertial wave propagation in geostrophic shear. *J. Phys. Oceanogr.*, **15**, 544–565, https://doi.org/10.1175/1520-0485(1985)015<0544:NIWPIG>2.0.CO;2.

——, 1986: The mean and near-inertial velocity fields in a warm-core ring. *J. Phys. Oceanogr.*, **16**, 1444–1461, https://doi.org/10.1175/1520-0485(1986)016<1444:TMANIV>2.0.CO;2.

Lenn, Y.-D., and Coauthors, 2009: Vertical mixing at intermediate depths in the Arctic boundary current. *Geophys. Res. Lett.*, **36**, L05601, https://doi.org/10.1029/2008GL036792.

Lincoln, B. J., T. P. Rippeth, Y.-D. Lenn, M. L. Timmermans, W. J. Williams, and S. Bacon, 2016: Wind-driven mixing at intermediate depths in an ice-free Arctic Ocean. *Geophys. Res. Lett.*, **43**, 9749–9756, https://doi.org/10.1002/2016GL070454.

Luketina, D. A., and J. Imberger, 2001: Determining turbulent kinetic energy dissipation from Batchelor curve fitting. *J. Atmos. Oceanic Technol.*, **18**, 100–113, https://doi.org/10.1175/1520-0426(2001)018<0100:DTKEDF>2.0.CO;2.

MacKinnon, J. A., and Coauthors, 2016: A tale of two spicy seas. *Oceanography*, **29** (2), 50–61, https://doi.org/10.5670/oceanog.2016.38.

Manley, T., and K. Hunkins, 1985: Mesoscale eddies of the Arctic Ocean. *J. Geophys. Res.*, **90**, 4911–4930, https://doi.org/10.1029/JC090iC03p04911.

May, B. D., and D. E. Kelley, 1997: Effect of baroclinicity on double-diffusive interleaving. *J. Phys. Oceanogr.*, **27**, 1997–2008, https://doi.org/10.1175/1520-0485(1997)027<1997:EOBODD>2.0.CO;2.

Maykut, G. A., and N. Untersteiner, 1971: Some results from a time-dependent thermodynamic model of sea ice. *J. Geophys. Res.*, **76**, 1550–1575, https://doi.org/10.1029/JC076i006p01550.

Melling, H., R. Lake, D. Topham, and D. Fissel, 1984: Oceanic thermal structure in the western Canadian Arctic. *Cont. Shelf Res.*, **3**, 233–258, https://doi.org/10.1016/0278-4343(84)90010-4.

Metzger, E. J., and Coauthors, 2014: US Navy operational global ocean and Arctic ice prediction systems. *Oceanography*, **27** (3), 32–43, https://doi.org/10.5670/oceanog.2014.66.

Meyer, A., I. Fer, A. Sundfjord, and A. K. Peterson, 2017: Mixing rates and vertical heat fluxes north of Svalbard from Arctic winter to spring. *J. Geophys. Res. Oceans*, **122**, 4569–4586, https://doi.org/10.1002/2016JC012441.

Muench, R. D., J. T. Gunn, T. E. Whitledge, P. Schlosser, and W. Smethie, 2000: An Arctic Ocean cold core eddy. *J. Geophys. Res.*, **105**, 23 997–24 006, https://doi.org/10.1029/2000JC000212.

Münchow, A., and E. C. Carmack, 1997: Synoptic flow and density observations near an Arctic shelf break. *J. Phys. Oceanogr.*, **27**, 1402–1419, https://doi.org/10.1175/1520-0485(1997)027<1402:SFADON>2.0.CO;2.

——, ——, and D. A. Huntley, 2000: Synoptic density and velocity observations of slope waters in the Chukchi and East-Siberian Seas. *J. Geophys. Res.*, **105**, 14 103–14 119, https://doi.org/10.1029/1999JC000002.

Neshyba, S., V. T. Neal, and W. Denner, 1971: Temperature and conductivity measurements under Ice Island T-3. *J. Geophys. Res.*, **76**, 8107–8120, https://doi.org/10.1029/JC076i033p08107.

Newton, J., K. Aagaard, and L. K. Coachman, 1974: Baroclinic eddies in the Arctic Ocean. *Deep-Sea Res. Oceanogr. Abstr.*, **21**, 707–719, https://doi.org/10.1016/0011-7471(74)90078-3.

Nikolopoulos, A., R. S. Pickart, P. S. Fratantoni, K. Shimada, D. J. Torres, and E. P. Jones, 2009: The western Arctic boundary current at 152°W: Structure, variability, and transport. *Deep-Sea Res. II*, **56**, 1164–1181, https://doi.org/10.1016/j.dsr2.2008.10.014.

Osborn, T. R., 1980: Estimates of the local rate of vertical diffusion from dissipation measurements. *J. Phys. Oceanogr.*, **10**, 83–89, https://doi.org/10.1175/1520-0485(1980)010<0083:EOTLRO>2.0.CO;2.

——, and C. S. Cox, 1972: Oceanic fine structure. *Geophys. Fluid Dyn.*, **3**, 321–345, https://doi.org/10.1080/03091927208236085.

Overland, J. E., and M. Wang, 2013: When will the summer Arctic be nearly sea ice free? *Geophys. Res. Lett.*, **40**, 2097–2101, https://doi.org/10.1002/grl.50316.

Padman, L., 1994: Momentum fluxes through sheared oceanic thermohaline steps. *J. Geophys. Res.*, **99**, 22 491–22 499, https://doi.org/10.1029/94JC01741.

——, and T. M. Dillon, 1987: Vertical heat fluxes through the Beaufort Sea thermohaline staircase. *J. Geophys. Res.*, **92**, 10 799–10 806, https://doi.org/10.1029/JC092iC10p10799.

——, and ——, 1988: On the horizontal extent of the Canada Basin thermohaline steps. *J. Phys. Oceanogr.*, **18**, 1458–1462, https://doi.org/10.1175/1520-0485(1988)018<1458:OTHEOT>2.0.CO;2.

——, and ——, 1989: Thermal microstructure and internal waves in the Canada Basin diffusive staircase. *Deep-Sea Res.*, **36**, 531–542, https://doi.org/10.1016/0198-0149(89)90004-6.

——, and ——, 1991: Turbulent mixing near the Yermak Plateau during the Coordinated Eastern Arctic Experiment. *J. Geophys. Res.*, **96**, 4769–4782, https://doi.org/10.1029/90JC02260.

——, M. D. Levine, T. Dillon, J. Morison, and R. Pinkel, 1990: Hydrography and microstructure of an Arctic cyclonic eddy. *J. Geophys. Res.*, **95**, 9411–9420, https://doi.org/10.1029/JC095iC06p09411.

Peters, H., M. Gregg, and J. Toole, 1988: On the parameterization of equatorial turbulence. *J. Geophys. Res.*, **93**, 1199–1218, https://doi.org/10.1029/JC093iC02p01199.

Peterson, A. K., I. Fer, M. G. McPhee, and A. Randelhoff, 2017: Turbulent heat and momentum fluxes in the upper ocean under Arctic sea ice. *J. Geophys. Res. Oceans*, **122**, 1439–1456, https://doi.org/10.1002/2016JC012283.

Pickart, R. S., 2004: Shelfbreak circulation in the Alaskan Beaufort Sea: Mean structure and variability. *J. Geophys. Res.*, **109**, C04024, https://doi.org/10.1029/2003JC001912.

——, and G. Stossmeister, 2008: Outflow of Pacific water from the Chukchi Sea to the Arctic Ocean. *Chin. J. Polar Oceanogr.*, **19**, 135–148.

——, T. J. Weingartner, L. J. Pratt, S. Zimmermann, and D. J. Torres, 2005: Flow of winter-transformed Pacific water into the western Arctic. *Deep-Sea Res. II*, **52**, 3175–3198, https://doi.org/10.1016/j.dsr2.2005.10.009.

Pinkel, R., 2005: Near-inertial wave propagation in the western Arctic. *J. Phys. Oceanogr.*, **35**, 645–665, https://doi.org/10.1175/JPO2715.1.

Pisareva, M. N., R. S. Pickart, M. Spall, C. Nobre, D. Torres, G. Moore, and T. E. Whitledge, 2015: Flow of Pacific water in the western Chukchi Sea: Results from the 2009 RUSALCA expedition. *Deep-Sea Res. I*, **105**, 53–73, https://doi.org/10.1016/j.dsr.2015.08.011.

Plueddemann, A., R. Krishfield, T. Takizawa, K. Hatakeyama, and S. Honjo, 1998: Upper ocean velocities in the Beaufort Gyre. *Geophys. Res. Lett.*, **25**, 183–186, https://doi.org/10.1029/97GL53638.

Polyakov, I. V., A. V. Pnyushkov, R. Rember, V. V. Ivanov, Y.-D. Lenn, L. Padman, and E. C. Carmack, 2012: Mooring-based observations of double-diffusive staircases over the Laptev Sea slope. *J. Phys. Oceanogr.*, **42**, 95–109, https://doi.org/10.1175/2011JPO4606.1.

Ruddick, B. R., 1992: Intrusive mixing in a Mediterranean salt lens—Intrusion slopes and dynamical mechanisms. *J. Phys. Oceanogr.*, **22**, 1274–1285, https://doi.org/10.1175/1520-0485(1992)022<1274:IMIAMS>2.0.CO;2.

——, and J. S. Turner, 1979: The vertical length scale of double-diffusive intrusions. *Deep-Sea Res.*, **26A**, 903–913, https://doi.org/10.1016/198-0149(79)90104-3.

——, and K. Richards, 2003: Oceanic thermohaline intrusions: Observations. *Prog. Oceanogr.*, **56**, 499–523, https://doi.org/10.1016/S0079-6611(03)00028-4.

——, A. Anis, and K. Thompson, 2000: Maximum likelihood spectral fitting: The Batchelor spectrum. *J. Atmos. Oceanic Technol.*, **17**, 1541–1555, https://doi.org/10.1175/1520-0426(2000)017<1541:MLSFTB>2.0.CO;2.

——, N. S. Oakey, and D. Hebert, 2010: Measuring lateral heat flux across a thermohaline front: A model and observational test. *J. Mar. Res.*, **68**, 523–539, https://doi.org/10.1357/002224010794657146.

Rudels, B., 2001: Arctic Basin circulation. *Encyclopedia of Ocean Sciences*, J. Steele, Ed., Academic Press, 177–187.

Shaw, P.-T., and S.-Y. Chao, 2003: Effects of a baroclinic current on a sinking dense water plume from a submarine canyon and heton shedding. *Deep-Sea Res. I*, **50**, 357–370, https://doi.org/10.1016/S0967-0637(03)00017-7.

Shimada, K., E. C. Carmack, K. Hatakeyama, and T. Takizawa, 2001: Varieties of shallow temperature maximum waters in the

western Canadian Basin of the Arctic Ocean. *Geophys. Res. Lett.*, **28**, 3441–3444, https://doi.org/10.1029/2001GL013168.

——, T. Kamoshida, M. Itoh, S. Nishino, E. Carmack, F. McLaughlin, S. Zimmermann, and A. Proshutinsky, 2006: Pacific Ocean inflow: Influence on catastrophic reduction of sea ice cover in the Arctic Ocean. *Geophys. Res. Lett.*, **33**, L08605, https://doi.org/10.1029/2005GL025624.

Shroyer, E. L., 2012: Turbulent kinetic energy dissipation in Barrow Canyon. *J. Phys. Oceanogr.*, **42**, 1012–1021, https://doi.org/10.1175/JPO-D-11-0184.1.

Sirevaag, A., and I. Fer, 2012: Vertical heat transfer in the Arctic Ocean: The role of double-diffusive mixing. *J. Geophys. Res. Oceans*, **117**, C07010, https://doi.org/10.1029/2012JC007910.

Smith, M., and Coauthors, 2018: Episodic reversal of autumn ice advance caused by release of ocean heat in the Beaufort Sea. *J. Geophys. Res. Oceans*, **123**, 3164–3185, https://doi.org/10.1002/2018JC013764.

Smyth, W. D., and S. Kimura, 2007: Instability and diapycnal momentum transport in a double-diffusive, stratified shear layer. *J. Phys. Oceanogr.*, **37**, 1551–1565, https://doi.org/10.1175/JPO3070.1.

Spall, M. A., R. S. Pickart, P. S. Fratantoni, and A. J. Plueddemann, 2008: Western Arctic shelfbreak eddies: Formation and transport. *J. Phys. Oceanogr.*, **38**, 1644–1668, https://doi.org/10.1175/2007JPO3829.1.

Stamp, A. P., G. O. Hughes, R. I. Nokes, and R. W. Griffiths, 1998: The coupling of waves and convection. *J. Fluid Mech.*, **372**, 231–271, https://doi.org/10.1017/S0022112098002304.

Steele, M., J. Morison, W. Ermold, I. Rigor, M. Ortmeyer, and K. Shimada, 2004: Circulation of summer Pacific halocline water in the Arctic Ocean. *J. Geophys. Res.*, **109**, C02027, https://doi.org/10.1029/2003JC002009.

Stern, M. E., 1967: Lateral mixing of water masses. *Deep-Sea Res.*, **14**, 747–753.

St. Laurent, L., and R. Schmitt, 1999: The contribution of salt fingers to vertical mixing in the North Atlantic Tracer Release Experiment. *J. Phys. Oceanogr.*, **29**, 1404–1424, https://doi.org/10.1175/1520-0485(1999)029<1404:TCOSFT>2.0.CO;2.

Sundfjord, A., I. Fer, Y. Kasajima, and H. Svendsen, 2007: Observations of turbulent mixing and hydrography in the marginal ice zone of the Barents Sea. *J. Geophys. Res.*, **112**, C05008, https://doi.org/10.1029/2006JC003524.

Timmermans, M.-L., 2015: The impact of stored solar heat on Arctic sea ice growth. *Geophys. Res. Lett.*, **42**, 6399–6406, https://doi.org/10.1002/2015GL064541.

——, and S. R. Jayne, 2016: The Arctic Ocean spices up. *J. Phys. Oceanogr.*, **46**, 1277–1284, https://doi.org/10.1175/JPO-D-16-0027.1.

——, J. Toole, R. Krishfield, and P. Winsor, 2008a: Ice-tethered profiler observations of the double-diffusive staircase in the Canada Basin thermocline. *J. Geophys. Res.*, **113**, C00A02, https://doi.org/10.1029/2008JC004829.

——, ——, A. Proshutinsky, R. Krishfield, and A. Plueddemann, 2008b: Eddies in the Canada Basin, Arctic Ocean, observed from ice-tethered profilers. *J. Phys. Oceanogr.*, **38**, 133–145, https://doi.org/10.1175/2007JPO3782.1.

——, and Coauthors, 2014: Mechanisms of Pacific summer water variability in the Arctic's central Canada Basin. *J. Geophys. Res. Oceans*, **119**, 7523–7548, https://doi.org/10.1002/2014JC010273.

Toole, J. M., M.-L. Timmermans, D. K. Perovich, R. A. Krishfield, A. Proshutinsky, and J. Richter-Menge, 2010: Influences of the ocean surface mixed layer and thermohaline stratification on Arctic sea ice in the central Canada Basin. *J. Geophys. Res.*, **115**, C10018, https://doi.org/10.1029/2009JC005660.

Turner, J. S., 1973: *Buoyancy Effects in Fluids.* Cambridge University Press, 367 pp.

——, 1974: Double-diffusive phenomena. *Annu. Rev. Fluid Mech.*, **6**, 37–55, https://doi.org/10.1146/annurev.fl.06.010174.000345.

——, 1978: Double-diffusive intrusions into a density gradient. *J. Geophys. Res.*, **83**, 2887–2901, https://doi.org/10.1029/JC083iC06p02887.

von Appen, W.-J., and R. S. Pickart, 2012: Two configurations of the western Arctic shelfbreak current in summer. *J. Phys. Oceanogr.*, **42**, 329–351, https://doi.org/10.1175/JPO-D-11-026.1.

Watanabe, E., 2011: Beaufort shelf break eddies and shelf-basin exchange of Pacific summer water in the western Arctic Ocean detected by satellite and modeling analyses. *J. Geophys. Res.*, **116**, C08034, https://doi.org/10.1029/2010JC006259.

Wesson, J. C., and M. C. Gregg, 1994: Mixing at Camarinal Sill in the Strait of Gibraltar. *J. Geophys. Res.*, **99**, 9847–9878, https://doi.org/10.1029/94JC00256.

Winters, K. B., and E. A. D'Asaro, 1996: Diascalar flux and the rate of fluid mixing. *J. Fluid Mech.*, **317**, 179–193, https://doi.org/10.1017/S0022112096000717.

Woodgate, R. A., T. Weingartner, and R. Lindsay, 2010: The 2007 Bering Strait oceanic heat flux and anomalous Arctic sea-ice retreat. *Geophys. Res. Lett.*, **37**, L01602, https://doi.org/10.1029/2009GL041621.

Zhao, M., M.-L. Timmermans, S. Cole, R. Krishfield, A. Proshutinsky, and J. Toole, 2014: Characterizing the eddy field in the Arctic Ocean halocline. *J. Geophys. Res. Oceans*, **119**, 8800–8817, https://doi.org/10.1002/2014JC010488.